Effects of model resolution and parameterizations on the simulations of clouds, precipitation, and their interactions with aerosols

Seoung Soo Lee[1], Zhanqing Li[1], Yuwei Zhang[1], Hyelim Yoo[2], Seungbum Kim[3], Byung-Gon Kim[4], Yong-Sang Choi[5]

[1]Earth System Science Interdisciplinary Center, University of Maryland, College Park, Maryland

[2]Earth Resources Technology, Inc., National Oceanic and Atmospheric Administration, College Park, Maryland

[3]Weather Impact Forecasts Team, Korea Meteorological Administration, Seoul, South Korea

[4]Department of Atmospheric Environmental Sciences, Gangneung-Wonju National University, Gangneung, Gang-Won do, South Korea

[5]Department of Environmental Science and Engineering, Ewha Womans University, Seoul, South Korea

Corresponding author: Seoung Soo Lee
Office: (303) 497-6615
Cell: (609) 375-6685
Fax: (303) 497-5318
E-mail: cumulss@gmail.com,slee1247@umd.edu

Abstract

This study investigates the effects of model resolution and microphysics parameterizations on the uncertainties or errors in the simulations of clouds, precipitation, and their interactions with aerosols using the Global Forecast System (GFS) model as one of the representative numerical weather prediction (NWP) models. For this investigation, we used the GFS model results and compare them with those from the cloud-system resolving model (CSRM) simulations as benchmark simulations that adopt a high resolution and full-fledged microphysical processes. These simulations were evaluated against observations and this evaluation demonstrated that the CSRM simulations can function as benchmark simulations. Substantially lower updrafts and associated cloud variables (e.g., cloud mass and condensation) were simulated by the GFS model compared to those simulated by the CSRM. This is mainly due to coarse resolution in the GFS model. This indicates that the parameterizations that represent sub-grid processes in the GFS model do not work well and thus need to be improved. Results here also indicate that the use of coarse resolution in the GFS model lowers the sensitivity of updrafts and cloud variables to increasing aerosol concentrations compared to the CSRM simulations. The parameterization of the saturation process plays an important role in the sensitivity of cloud variables to aerosol concentrations while the parameterization of the sedimentation process has a substantial impact on how cloud variables are distributed vertically. The variation in cloud variables with resolution is much greater and contributes to the discrepancy between the GFS and CSRM simulations to a much greater degree than what happens with varying microphysics parameterizations.

1. Introduction

The treatment of clouds and precipitation and their interactions with aerosols in the NWP models is likely a major source of errors in the simulations of the water and energy cycles (Sundqvist et al., 1989; Randall et al., 2006; Seifert et al., 2012). The NWP community has recognized that the accurate representation of clouds, precipitation, and cloud-aerosol-precipitation interactions (CAPI) is important for the improvement of the NWP models and thus, some of these models have started to improve the representation by considering CAPI (Morcrette et al., 2011; Sudhakar et al., 2016).

CAPI may not have a substantial impact on the total precipitation amount but they do affect the temporal and spatial variabilities of precipitation (Li et al., 2011; van den Heever et al., 2011; Seifert et al., 2012; Lee and Feingold, 2013; Fan et al., 2013; Lee et al., 2014), whose importance increases as the temporal/spatial scales of forecast decrease. The distribution of extreme precipitation events such as droughts and floods, closely linked to the spatiotemporal variability, has important social and economic implications.

In recent years, resolution in the NWP models has increased to the point that the traditional cumulus parameterization schemes may no longer work properly. Motivated by this, scale-aware cumulus parameterization schemes (e.g., Bogenschutz and Krueger, 2013; Thayer-Calder et al., 2015; Griffin and Larson, 2016) are being implemented into these models of different resolutions for better representation of clouds and precipitation. These scale-aware schemes, which represent sub-grid-scale dynamic processes (e.g., cloud-scale updrafts and downdrafts) that are associated with cloud convection as the traditional cumulus parameterizations do, are designed to be applied to the increased resolution in the NWP models.

The uncertainties or the errors in the simulations of clouds, precipitation, and CAPI in the NWP models may be incurred both from microphysics parameterizations and from model resolution. The implementation of the cloud microphysics such as the two-moment (e.g. Morrison and Gettelman, 2008; Morrison et al., 2009) and scale-aware schemes are intended to reduce these uncertainties. It is important to first understand and quantify the uncertainties associated with the two-moment scheme and how model resolution creates the uncertainties, as well as the relative significance between the uncertainties associated with the two-moment scheme and those created by resolution. This understanding and quantification can provide us with a guideline on how to represent microphysics in the two-moment schemes and sub-grid processes in the scale-aware schemes for the efficient reduction of the uncertainties in the NWP models. Note that the representation of sub-grid processes requires information on the contribution of resolution to the uncertainties and, in this study, we focus on the two-moment scheme developed by Morrison and Gettelman (2008) and Morrison et al. (2009), which is referred to as the MG scheme, henceforth.

Fan et al. (2012) and Khain et al. (2015) have shown that the parameterizations of three key microphysical processes (i.e., saturation, collection, and sedimentation) in microphysical schemes act as a main source of errors in the simulation of clouds, precipitation, and CAPI. We try to identify and quantify the errors or the uncertainties through comparisons between simulations with parameterizations of the three key processes in the MG scheme and the CSRM simulations with full-fledged microphysical processes. Regarding the understanding of the uncertainties arising from the choice of resolution, we also perform comparisons between the high-resolution CSRM simulations and the low-resolution simulations, and do additional comparisons with the GFS simulations. This helps gain an understanding of how the microphysical representation and coarse resolution in the GFS model (as compared to those in the CSRM) contribute to the uncertainties in the GFS simulations of clouds and precipitation by accounting for CAPI. Here, the CSRM simulations act as benchmark simulations by representing microphysical processes with high-level sophistication and by resolving cloud-scale physical and dynamic processes with a high resolution.

2. Models

2.1 The CSRM

The Advanced Research Weather Research and Forecasting (ARW) model, a non-hydrostatic compressible model, is the CSRM selected for use in this study. A fifth-order monotonic advection scheme is used for the advection of cloud variables (Wang et al., 2009). The ARW model considers radiation processes by adopting the Rapid Radiation Transfer Model for General Circulation Models (RRTMG) (Fouquart and Bonnel, 1980; Mlawer et al., 1997). The effective sizes of hydrometeors, which vary with varying aerosol properties, are calculated in a microphysics scheme that is adopted by this study and described below and the calculated sizes are transferred to the RRTMG. Then, the effects of the effective sizes of hydrometeors on radiation are calculated in the RRTMG. The ARW model considers the sub-grid-scale turbulence by adopting 1.5-order turbulence kinetic energy closure (Basu et al., 1998).

For an assessment of the uncertainties in the MG scheme, which is a type of a bulk scheme, we need to use microphysics schemes that are much more sophisticated than the MG scheme. Through extensive comparisons between various types of bin schemes and bulk schemes, Fan et al. (2012) and Khain et al. (2015) have concluded that the use of bin schemes or bin-bulk schemes is desirable for reasonable simulations of clouds, precipitation, and their interactions with aerosols. This is because these schemes do not use a saturation adjustment, a mass-weight mean terminal velocity, or constant collection efficiencies that have been used in bulk schemes. Instead, bin schemes use predicted supersaturation levels, and terminal velocities and collection efficiencies that vary with the sizes of hydrometeors. Based on the work by Fan et al. (2012) and Khain et al. (2015), this study considers bin schemes to be a full-fledged microphysics schemes against which the uncertainties in the MG scheme can be assessed. Hence, a bin scheme is adopted in the CSRM used here.

The bin scheme adopted by the CSRM is based on the Hebrew University Cloud Model described by Khain and Lynn (2009). The bin scheme solves a system of kinetic equations for the size distribution functions of water drops, ice crystals (plate, columnar and branch types), snow aggregates, graupel and hail, as well as cloud condensation nuclei. Each size distribution is represented by 33 mass-doubling bins, i.e., the mass of a particle m_k in the k^{th} bin is $m_k = 2m_{k-1}$.

As stated in introduction, this study focuses on the uncertainties or errors in the simulations of clouds, precipitation, and CAPI themselves. This means that the examination of the uncertainties in the simulations of aerosol physics and chemistry is out of scope of this study. Hence, in this study, instead of simulating aerosol physics and chemistry explicitly, initial aerosol physical and chemical properties (i.e., aerosol chemical composition and size distribution) are prescribed. Then, aerosol size distribution (or aerosol number concentration in each size bin) evolves only through cloud processes (as described below) but not through aerosol physical and chemical processes. During the evolution, the prescribed aerosol composition is assumed not to vary.

In this study, it is assumed that aerosol particles are composed of ammonium sulfate. The aerosol size distribution evolves prognostically with sinks and sources, which include advection, droplet nucleation, and aerosol regeneration from droplet evaporation (Fan et al., 2009). Aerosol activation is calculated according to the Köhler theory, i.e., aerosol particles with radii exceeding the critical value at a grid point are activated to become droplets based on predicted supersaturation, and the corresponding bins of the aerosol spectra are emptied. After activation, the aerosol mass is transported within hydrometeors by collision-coalescence and removed from the atmosphere once hydrometeors that contain aerosols reach the surface. Aerosol particles return to the atmosphere upon evaporation or the sublimation of hydrometeors that contain them.

2.2 The GFS model

The GFS model is a global NWP model that is run by the National Oceanic and Atmospheric Administration (NOAA). The GFS model has 64 vertical sigma-pressure hybrid layers and a T382 (~ 35 km) horizontal resolution. Output fields for a forecast generated at 3-hour intervals (i.e. at 03, 06, 09, 12, 15, 18, 21, 24 universal coordinated time, or Z), starting from the control time of 00Z, are used for this study.

The GFS model posts parameters for 21 vertically different layers. From the surface (1000 hPa) to the 900-hPa level, the vertical resolution is 25 hPa. At pressures less than 900 hPa, there are 16 levels at a 50-hPa resolution up to 100 hPa. The cloud phase is determined by the mean temperature (Tc) of a cloud layer which is defined as the average of temperatures at the top and bottom of a cloud layer. If Tc is less than 258.16 K, the cloud layer is an ice cloud; otherwise, it is a water cloud.

A prognostic condensate scheme by Moorthi et al. (2001) has been used to parameterize clouds in the GFS model. In this scheme, cloud mass, one of the representative cloud variables, evolves by considering the cloud-mass advection, diffusion and conversion to precipitation, and the diagnosed sub-grid and grid-scale phase-transition processes (e.g., condensation and evaporation). Here, cloud mass is represented by cloud liquid content (CLC) or cloud ice content (CIC), depending on temperature, and cloud liquid (cloud ice) represents droplets (ice crystals). The grid-scale phase-transition processes are calculated based on Sundqvist et al. (1989) and Zhao and Carr (1997), while the sub-grid transition processes are calculated based on a cumulus parameterization that adopts the mass-flux approach. This cumulus parameterization was developed by Moorthi et al. (2001) based on a simplified Arakawa-Schubert scheme (Pan and Wu, 1995).

3. The cases

3.1 The Seoul case

A mesoscale convective system (MCS) was observed over Seoul, Korea (37.57^{o}N, 126.97^{o}E; 0900 local solar time (LST) 26 July 2011–0900 LST 27 July 2011). This case, referred to as the Seoul case, involved heavy rainfall with a maximum precipitation rate of ~150 mm h^{-1}. This heavy rainfall caused flash floods and landslides on a mountain at the southern flank of the city, leading to the deaths of 60 people.

At 0900 LST July 26th 2011, favorable synoptic-scale features for the development of heavy rainfall over Seoul were observed. The western Pacific subtropical high (WPSH) was located over the southeast of Korea and Japan, and there was a low-pressure trough over north China (Figure 1a). Low-level jets between the flank of the WPSH and the low-pressure system brought warm, moist air from the Yellow Sea to the Korean Peninsula (Figure 1b). Transport of warm and moist air by the southwesterly low-level jet is an important condition for the development of heavy rainfall events over Seoul (Hwang and Lee, 1993; Sun and Lee, 2002).

3.2 The Houston case

An MCS was observed over Houston, Texas (29.42^{o}N, 94.45^{o}W; 0700 LST 18 July 2013–0400 LST 19 July 2013). The Houston case involved moderate rainfall with a maximum precipitation rate of ~50 mm h^{-1}.

At 0500 LST, two hours before the initiation of convection, the low-level wind in and around Houston was southerly (Figure 1c), favoring the transport of water vapor from the Gulf of Mexico to the Houston area. Associated with this, the environmental convective available potential energy (CAPE) (Figure 1d) in and around Houston along the coastline was high (as represented by red areas in Figure 1d). The high CAPE provided a favorable condition for the development of the MCS.

4. Simulations

4.1 The CSRM simulations

Using the ARW model and its bin scheme, a three-dimensional CSRM simulation of the observed MCS was performed over the MCS period for each of the cases.

Initial and boundary conditions, which represent the synoptic features, for the control run are derived from the National Centers for Environmental Prediction GFS final (FNL) analysis. Since the FNL analysis is based on environmental conditions that are produced by the GFS model and thus for each of the cases, there are basically no differences in the synoptic condition between the CSRM simulations and the GFS simulations that are described in the following Section 4.2. The open lateral boundary condition is adopted in the control run. This enables the advection of the synoptic condition into and out of a domain in the CSRM simulations to occur through the boundary of the domain, which emulates the advection in the GFS simulations. All experiments employ a prognostic surface skin temperature scheme (Zeng and Beljaars, 2005) and a revised roughness length formulation (Donelan et al., 2004).

The control run for each of the cases consists of a domain with a Lambert conformal map projection. The domain is marked by the rectangle for the Seoul case in Figure 2a and the domain for the Houston case is shown in Figure 2b. While the control run for the Seoul case is referred to as “the control-Seoul run”, the control run for the Houston case is referred to as “the control-Houston run”, henceforth. The domain for the Seoul (Houston) case covers the Seoul (Houston) area and to resolve cloud-scale processes, a 500-m horizontal resolution is applied to the domain. The domain has 41 vertical layers with the vertical resolution ranging from 70 m near the surface to 800 m at the model top (~50 hPa). Note that the cumulus parameterization scheme is not used in this domain where cloud-scale convection and associated convective rainfall generation are assumed to be explicitly resolved. Based on observations, the aerosol concentration at the surface at the first time step is set at 5500 (1500) cm^{-3} for the Seoul (Houston) case. Above the top of the planetary boundary layer (PBL) around 2 km, the aerosol concentration reduces exponentially.

To examine and isolate CAPI, i.e., the effect of increasing the loading of aerosols on clouds and precipitation, the control run is repeated with the aerosol concentration at the first time step reduced by a factor of 10. This factor is based on observations showing that that reduction in aerosol loading between polluted days and clean days is generally tenfold over Seoul and Houston(Lance et al., 2009; Kim et al., 2014). This simulation is referred to as the low-aerosol-Seoul run for the Seoul case and the low-aerosol-Houston run for the Houston case. Since the control-Seoul run and the control-Houston run involve higher aerosol concentrations than the low-aerosol-Seoul run and the low-aerosol-Houston run, respectively, for naming purposes, the control-Seoul run and the control-Houston run are also referred to as the high-aerosol-Seoul run and the high-aerosol-Houston run, respectively.

In addition to the simulations described above, more simulations were performed to fulfill the goals of this study (Table 1). Details of those simulations are given in the following sections.

4.2 The GFS simulations

Note that the GFS produces the forecast data over the globe and for this study, we use the data only during the MCS period and only at grid points in the domain for each case. Stated differently, the spatial scale or the extent of the analysis area is identical between the CSRM simulations and the GFS simulations, although the number of grid points in the area or the domain is different between the CSRM simulations and the GFS simulations due to differences in resolution between those simulations. We collect GFS data in the domain and then average the data over those grid points at each of the GFS time steps for each of the cases. For the comparison between the GFS and CSRM simulations at specific time steps over the MCS period, these averaged data are compared to the CSRM simulations for each of those steps. In case the time and domain-averaged GFS data are compared to the CSRM counterparts, these averaged data are averaged again over the MCS period and compared to their CSRM counterparts.

5. Results

5.1 Test on the effects of resolution on the simulations of clouds, precipitation, and CAPI

5.1.1 CLC and CIC

To test the effects of resolution on the simulations of clouds, precipitation, and their interactions with aerosols, we repeat the standard CSRM runs at the 500-m resolution (i.e., the high-aerosol-Seoul run, the low-aerosol-Seoul run, the high-aerosol-Houston run, and the low-aerosol-Houston run) by using 15- and 35-km resolutions instead. These resolutions are similar to those generally adopted by current NWP models (e.g., the GFS model). To isolate the effects of resolution on the simulations of clouds, precipitation, and their interactions with aerosols, only resolution varies among the CSRM runs at the fine resolution and the repeated runs at the coarse resolutions here and these runs have an identical model setup except for resolution. For the identical setup, as an example, we do not apply the convection parameterizations (e.g., cumulus parameterizations) to the repeated runs, since the convection parameterizations are not applied to the CSRM runs. Hence, cloud variables (e.g., the updraft speed) are not diagnosed by convection parameterizations but predicted in both the CSRM runs and the repeated runs. With the identical setup except for resolution, the comparisons between the CSRM simulations and the repeated simulations can isolate the pure effects of the use of coarse resolution on clouds, precipitation, and their interactions with aerosol.

The repeated simulations at the 15-km resolution are referred to as the high-aerosol-15-Seoul run, the low-aerosol-15-Seoul run, the high-aerosol-15-Houston run, and the low-aerosol-15-Houston run, while the repeated simulations at the 35-km resolution are referred to as the high-aerosol-35-Seoul run, the low-aerosol-35-Seoul run, the high-aerosol-35-Houston run, and the low-aerosol-35-Houston run. In this study, simulations whose name includes "high-aerosol" represent the polluted scenario, while those whose name includes "low-aerosol" represent the clean scenario. In the following, we describe results from the standard and repeated simulations. For the Houston case, no clouds form at the 35-km resolution, so the description of results is only done for results at the 15-km resolution.

Figures 3a and 3b show the vertical distributions of the time- and domain-averaged CLC in the simulations for the Seoul case and the Houston case, respectively. Figures 4a and 4b show the vertical distributions of the time- and domain-averaged CIC in the simulations for the Seoul case and the Houston case, respectively. There are increases in the cloud mass (represented by CLC and CIC) with increasing aerosol concentration between the polluted scenario and the clean scenario not only for both the Seoul and Houston cases but also at all resolutions considered. The cloud mass is substantially less at the 15- and 35-km resolutions compared to that in the simulations at the 500-m resolution. In addition, increases in the cloud mass with increasing aerosol concentration reduce substantially as resolution coarsens. At the 500-m resolution, on average, there is about a ~30–50% increase in cloud mass, while at the 15- or 35-km resolutions, there is only a ~2–5% increase in cloud mass in both cases.

For both the Seoul and Houston cases, comparisons between the cloud mass produced by the GFS simulations and that produced by the ARW simulations show that the GFS-simulated cloud mass is similar to that in the ARW simulations at the 15- and 35-km resolutions. However, the GFS-simulated cloud mass is much smaller than that in the ARW simulations at the 500-m resolution, i.e., the CSRM simulations. This suggests that coarse resolution used in the GFS simulations is an important cause of the differences in cloud mass between the CSRM simulations and the GFS simulations.

5.1.2 Liquid water path (LWP) and ice water path (IWP)

Figures 5a and 5b show the time series of the domain-averaged LWP and IWP for the Seoul case while Figures 6a and 6b show the same for the Houston case. Note that LWP and IWP are the vertical integrals of CLC and CIC, respectively. Consequently, the same behavior as that of CLC and CIC is seen, namely, there are increases in LWP and IWP with increasing aerosol concentrations between the polluted and clean scenarios at all resolutions, while there are less LWP and IWP with the use of the 15- and 35-km resolutions compared to using the 500-m resolution. Also, the sensitivity of LWP and IWP to increasing aerosol concentrations reduces significantly as resolution coarsens.

In Figures 5 and 6, satellite-observed LWP and IWP for both cases follow reasonably well their CSRM-simulated counterparts for the polluted scenario. This shows that the CSRM simulations, which are performed with the 500-m resolution, perform well and can thus represent benchmark simulations. The GFS-produced LWP and IWP are similar to those in the ARW simulations at the 15- and 35-km resolutions and are much smaller in magnitude than those from the CSRM simulations and observations. Hence, the discrepancy in LWP and IWP between the GFS simulations and the CSRM simulations or that between the GFS simulations and observations is closely linked to coarse resolution adopted by the GFS simulations. Taking the CSRM simulations as benchmark simulations, we see that the GFS simulations underestimate the cloud mass compared to observations mainly due to coarse resolution adopted by the GFS model.

Among the ARW simulations, the sensitivity of the cloud mass to increasing aerosol concentrations reduces considerably with coarsening resolution. CSRM simulations are benchmark simulations so the sensitivity in the CSRM simulations is the benchmark sensitivity. Note that the GFS simulation results and the ARW simulations at the coarse resolutions of 15 and 35 km are similar. Their sensitivities are thus also likely similar, i.e., the sensitivity of the cloud mass to increasing aerosol concentrations in the GFS simulation is likely to be underestimated compared to the benchmark sensitivity of the CSRM simulations.

5.1.3 Updrafts, condensation, and deposition

To understand the response of the cloud mass to increasing aerosol concentrations, and the variation in the cloud mass and its response to increasing aerosol concentrations with varying resolution as shown in

Figures 3, 4, 5, and 6, we calculate updraft mass fluxes since these fluxes control supersaturation that in turn controls condensation and deposition as key determination factors for the cloud mass. Updraft mass fluxes are obtained by multiplying the predicted updraft speed by air density. Since there are negligible differences in air density among the ARW simulations, most of differences in updraft mass fluxes among the simulations are caused by differences in the updraft speed or updrafts. Those differences in air density are in general ~ two orders of magnitude smaller than those in the updraft speed or updrafts. We also obtain condensation and deposition rates. The vertical distributions of the time- and domain-averaged updraft mass fluxes, condensation rates, and deposition rates for the Seoul and Houston cases are shown in Figures 7, 8, and 9, respectively. Here, condensation and deposition rates are defined as the rates of changes in liquid mass and ice mass in a unit volume of air and for a unit time due to condensation and deposition on the surface of hydrometeors, respectively.

As seen for the cloud mass, updraft mass fluxes, and condensation and deposition rates increase with increasing aerosol concentrations between the polluted scenario and the clean scenario at all resolutions and for all cases considered. Increasing aerosol concentrations alter cloud microphysical properties such as drop size and autoconversion. Aerosol-induced changes in autoconversion in turn increase cloud-liquid mass as a source of evaporation and freezing. Numerous studies (e.g., Khain et al., 2005; Seifert and Beheng, 2006; Tao et al., 2007, 2012; van den Heever and Cotton, 2007; Storer et al., 2010; Lee et al., 2013, 2017) have shown that aerosol-induced increases in cloud-liquid mass and associated increases in freezing of cloud liquid enhance the freezing-related latent heating and thus parcel buoyancy, and this invigorates convection or increases updraft mass fluxes. Those studies have also shown that the aerosol-induced increases in cloud-liquid mass and associated increases in the evaporation of cloud liquid enhance the evaporation-related latent cooling and thus negative buoyancy. This intensifies downdrafts and after reaching the surface, the intensified downdrafts spread out toward the surrounding warm air to form intensified gust fronts and then, to uplift the warm air more strongly. More strongly uplifted warm air leads to invigorated convection or increased updraft mass fluxes. These freezing- and evaporation-related invigoration mechanisms are operative to induce the aerosol-induced enhancement of updraft mass fluxes, condensation, and deposition in this study.

Aerosol-induced percentage increases in updraft mass fluxes, and deposition and condensation rates at the 500-m resolution between the polluted scenario and the clean scenario are approximately one order of magnitude greater than those at the 15- and 35-km resolutions. Stated differently, the sensitivity of updraft mass fluxes to increasing aerosol concentrations reduces substantially with coarsening resolution and due to this, the sensitivity of deposition and condensation rates, and thus the cloud mass, to increasing aerosol concentrations also reduces substantially with coarsening resolution. Similar to the situation with the cloud mass, the GFS-produced updraft mass fluxes are much smaller than those produced by the ARW simulations at the 500-m resolution (or the CSRM simulations) and similar to those produced by the ARW simulations at the 15- and 35-km resolutions (Figure 7). Hence, taking the CSRM simulations as benchmark simulations, the updraft mass fluxes (and thus the cloud mass) are underestimated in the GFS simulations and the ARW simulations at the 15- and 35-km resolutions. This underestimation is closely linked to the discrepancy in resolution between the GFS simulations and the CSRM simulations or between the ARW simulations at the 15- and 35-km resolutions and the CSRM simulations. Taking the sensitivity of updraft mass fluxes to increasing aerosol concentrations in the CSRM simulations as the benchmark sensitivity, the GFS simulations likely also underestimate the sensitivity, considering the similarity in results between the ARW simulations at the 15- and 35-km resolutions and the GFS simulations. Since the current GFS model does not consider pathways through which increasing aerosol concentrations interact with updraft mass fluxes, this probable underestimation of the sensitivity is even more likely. Note that the ARW simulations which are at the 15- and 35-km resolutions and underestimate updrafts themselves, even with the consideration of those pathways, result in the much weaker sensitivity at the coarse resolutions as compared to that in the CSRM simulations. Hence, even though those pathways are implemented into the GFS model, the underestimated updrafts in the GFS simulations are likely to result in the weak sensitivity, unless the cumulus parameterization which represents updrafts in the GFS model is further developed to prevent the underestimation of updrafts.

Figure 10 shows the frequency distribution of updrafts over the updraft speed, which is normalized over the domain and the simulation period. We first calculate the frequency over the domain at each time step and in each discretized updraft bin. The frequency in each bin and at each time step is then divided by the total number of grid points in the whole domain. The normalized frequency at each time step is summed over all of the time steps in each updraft bin. This sum is divided by the total number of time steps as the final step in the normalization process. With coarsening resolution, the normalized frequency of weak updrafts with speeds less than ~2 m s^{-1} increases for both scenarios in both cases. However, the normalized frequency of strong updrafts with speeds greater than ~2 m s^{-1} reduces with coarsening resolution. The frequency shift from high-level updraft speeds to low-level speeds leads to a reduction in the mean updrafts with coarsening resolution for both scenarios in both cases.

The updraft frequency is greater in the polluted scenario than in the clean scenario at all resolutions and for all cases. The overall difference in the frequency between the scenarios reduces with coarsening resolution. This is associated with the reduction in the sensitivity of the averaged updrafts to increasing aerosol concentrations with coarsening resolution. In particular, the difference in the frequency for weak updrafts (speeds less than ~2 m s^{-1}) between the scenarios does not vary much with coarsening resolution. On average, the percentage difference for weak updrafts is less than 2–3% at all resolutions. However, the difference for strong updrafts varies significantly with varying resolution. The mean difference for strong updrafts varies from ~30–60% for the 500-m resolution to less than ~5–6 % for the 15- and 35-km resolutions. Analyses of the updraft frequency here suggest that strong updrafts are more sensitive to aerosol-induced invigoration of convection than weak updrafts. The variation in the sensitivity of the averaged updrafts to increasing aerosol concentrations at varying resolution is associated more with the variation of the response of strong updrafts to aerosol-induced invigoration at varying resolution than with that of weak updrafts. Another point to make here is that the frequency of weak updrafts is overestimated while that of strong updrafts is underestimated at coarse resolution compared to the frequencies in the fine-resolution CSRM simulations.

5.1.4 Evaporation and precipitation distributions

Aerosol-induced increases in evaporation and associated cooling affect downdrafts, and changes in downdrafts in turn affect gust fronts. Aerosol-induced changes in the intensity of gust fronts affect the organization of cloud systems, which is characterized by cloud-cell spatiotemporal distributions. In general, aerosol-induced greater increases in evaporation result in aerosol-induced greater changes in the intensity of gust fronts and in cloud system organization (Tao et al., 2007, 2012; van den Heever and Cotton, 2007; Storer et al., 2010; Lee et al., 2013, 2017).

Considering that individual cloud cells act as individual sources of precipitation, aerosol-induced changes in the cloud system organization can alter precipitation spatiotemporal distributions, which play an important role in hydrological circulations. It is thus important to examine how the response of evaporation to increasing aerosol concentrations varies with varying resolution, i.e., to see how coarse resolution affects the quality of simulations of aerosol effects on hydrological circulations. Motivated by this, evaporation rates are obtained and are shown in Figure 11. Here, evaporation rate is defined as the rate of changes in liquid mass in a unit volume of air and for a unit time due to evaporation on the surface of hydrometeors.

As seen in the above-described variables, evaporation rates increase as the aerosol concentration increases and the sensitivity of the evaporation rate to increasing aerosol concentrations reduces with coarsening resolution among the ARW simulations. This suggests that the sensitivities of the cloud system organization and precipitation distributions to increasing aerosol concentrations likely also reduce with coarsening resolution, as reported in the previous studies (e.g., Tao et al., 2007, 2012; van den Heever and Cotton, 2007; Storer et al., 2010; Lee et al., 2013, 2017). This is confirmed by the distribution of normalized precipitation frequency over precipitation rates shown in Figure 12. Similar to the normalization for the updraft frequency, we first calculate the frequency of surface precipitation rates at each time step and in each discretized precipitation rate bin. The frequency in each bin and at each time step is then divided by the total number of grid points at the surface. The normalized frequency at each time step is summed over all of the time steps. This sum is divided by the total number of time steps as the final step in the normalization process. Figure 12 shows that due to the reduction in the sensitivity of evaporative cooling to increasing the aerosol concentration as resolution coarsens, differences in the distribution of precipitation frequency between the polluted scenario and the clean scenario reduce substantially as resolution coarsens. Taking the 500-m resolution CSRM simulations as benchmark simulations, this suggests that the coarse-resolution GFS simulations likely underestimate the sensitivity of evaporative cooling, cloud system organization, and precipitation distributions to increasing aerosol concentrations.

5.2 Test on the effects of microphysics parameterizations on the simulations of clouds, precipitation, and CAPI

As mentioned previously, among microphysical processes, saturation, sedimentation, and collection processes are those whose parameterizations are a main cause of errors in the simulation of clouds, precipitation, and CAPI. Motivated by this, we focus on these three microphysical processes for testing the effects of microphysics parameterizations on the simulations of clouds, precipitation, and CAPI. As a preliminary step to this test, we first focus on the effects of microphysics parameterizations on the simulation of the cloud mass, which plays a key role in cloud radiative properties and precipitation. Based on Figures 3 and 4, we focus on the CLC, which accounts for the bulk of the total cloud mass.

Figure 13 shows the vertical distributions of the time- and domain-averaged CLC. In Figure 13a, solid red and black lines represent the high-aerosol-Seoul run and the low-aerosol-Seoul run, respectively, while in Figure 13b, those lines represent the high-aerosol-Houston run and the low-aerosol-Houston run, respectively. Note that these runs shown in the figure are performed using the bin scheme and the 500-m resolution. These simulations were repeated with the Morrison two-moment scheme. These repeated simulations using the MG scheme, referred to as the high-aerosol-MG-Seoul run, the low-aerosol-MG-Seoul run, the high-aerosol-MG-Houston run and the low-aerosol-MG-Houston run, are represented by solid yellow and green lines in Figure 13. Between the high-aerosol and low-aerosol runs using the MG scheme for the two cases, there is an increase in CLC with increasing aerosol concentration. However, this increase is much smaller than that between the high-aerosol and low-aerosol runs using the bin scheme for the two cases. In addition, there is a significant difference in the shape of the vertical profile of CLC between the simulations with the MG scheme and those with the bin scheme for both cases. Here, the shape is represented by the peak value of CLC and the altitude of the peak value in the vertical profile. The peak value is higher in the simulations with the bin scheme than in the simulations with the MG scheme for each of the polluted and clean scenarios. The altitude of the peak value is lower in the simulations with the bin scheme than in the simulations with the MG scheme. For the Seoul (Houston) case, the altitude is ~2 (3) km in the simulations with the bin scheme, while it is ~5 km in those with the MG scheme.

We next test how the parameterization of saturation processes affects the simulations by comparing the supersaturation prediction in the bin scheme to the saturation adjustment in the MG scheme. To do this, the simulations with the bin scheme are repeated after replacing the supersaturation prediction in the bin scheme with the saturation adjustment in the MG scheme. These repeated simulations are referred to as the high-aerosol-sat-Seoul run, the low-aerosol-sat-Seoul run, the high-aerosol-sat-Houston run, and the low-aerosol-sat-Houston run. The high-aerosol-sat-Seoul run and the low-aerosol-sat-Seoul run for the Seoul case and the high-aerosol-sat-Houston run and the low-aerosol-sat-Houston run for the Houston case are represented by dashed lines in Figure 13. As in the other simulations, there is an increase in CLC with increasing aerosol concentrations between the high-aerosol-sat and the low-aerosol-sat runs for the two cases. However, this increase is much smaller than that between the high-aerosol and low-aerosol runs for the two cases, but is similar to that between the high-aerosol-MG and low-aerosol-MG runs for the two cases. This suggests that the sensitivity of the CLC to increasing aerosol concentrations is affected by the parameterization of the saturation process and that the use of the saturation adjustment reduces the sensitivity compared to using the supersaturation prediction.

The high-aerosol-sat-Seoul run, the low-aerosol-sat-Seoul run, the high-aerosol-sat-Houston run, and the low-aerosol-sat-Houston run are repeated by replacing the bin-scheme sedimentation with the sedimentation from the MG scheme as a way of testing the effects of the parameterization of sedimentation on the simulations. These repeated runs are referred to as the high-aerosol-sed-Seoul run, the low-aerosol-sed-Seoul run, the high-aerosol-sed-Houston run, and the low-aerosol-sed-Houston run. These runs are identical to the high-aerosol-Seoul run, the low-aerosol-Seoul run, the high-aerosol-Houston run and the low-aerosol-Houston run, respectively, except for the parameterization of the saturation and sedimentation processes. As mentioned previously, terminal velocities vary as hydrometeor sizes vary in the bin scheme, while the MG scheme adopts mass-weight mean terminal velocities for the calculation of the sedimentation process.

The vertical distributions of the CLC in the high-aerosol-sed-Seoul run, the low-aerosol-sed-Seoul run, the high-aerosol-sed-Houston run, and the low-aerosol-sed-Houston run are represented by dashed lines in Figure 14. Comparisons between the pair of high-aerosol-sed and low-aerosol-sed runs for the two cases and the pair of high-aerosol-MG and low-aerosol-MG runs for the two cases show that not only the increases in the CLC with increasing aerosol concentrations but also the shapes of the vertical distribution of the CLC in the high-aerosol-sed and low-aerosol-sed runs for the two cases are similar to those in the high-aerosol-MG and low-aerosol-MG runs for the two cases. This demonstrates that differences in the shape of the vertical profile of CLC between the bin-scheme simulations and the MG-scheme simulations are not explained by differences in the representation of the saturation process alone. This also demonstrates that the representation of the sedimentation process plays an important role in generating the differences in the shape of the vertical profile of CLC.

In Figure 14, we still see differences in the vertical profiles of CLC between the high-aerosol-sed-Seoul and high-aerosol-MG-Seoul runs, and between the low-aerosol-sed-Seoul and low-aerosol-MG-

Seoul runs, as well as between the high-aerosol-sed-Houston and high-aerosol-MG-Houston runs, and between the low-aerosol-sed-Houston and low-aerosol-MG-Houston runs. To understand the cause of these differences, the high-aerosol-sed-Seoul run, the low-aerosol-sed-Seoul run, the high-aerosol-sed-Houston run, and the low-aerosol-sed-Houston run are repeated again with the MG-scheme collection process. These repeated runs are referred to as the high-aerosol-col-Seoul run, the low-aerosol-col-Seoul run, the high-aerosol-col-Houston run, and the low-aerosol-col-Houston run. These runs are identical to the high-aerosol-Seoul run, the low-aerosol run-Seoul, the high-aerosol-Houston run, and the low-aerosol-Houston run, respectively, except for the parameterization of the saturation, sedimentation, and collection processes. As mentioned previously, collection efficiencies vary as hydrometeor sizes vary in the bin scheme, while the MG scheme uses constant collection efficiencies.

As seen in Figure 15, the remaining differences between the high-aerosol-col-Seoul and high-aerosol-MG-Seoul runs and between the low-aerosol-col-Seoul and low-aerosol-MG-Seoul runs, as well as between the high-aerosol-col-Houston and high-aerosol-MG-Houston runs, and between the low-aerosol-col-Houston and low-aerosol-MG-Houston runs nearly disappear. This demonstrates with fairly good confidence that differences between the high-aerosol-Seoul run (the high-aerosol-Houston run) and the high-aerosol-MG-Seoul run (the high-aerosol-MG-Houston run) or between the low-aerosol-Seoul run (the low-aerosol-Houston run) and the low-aerosol-MG-Seoul run (the low-aerosol-MG-Houston run) are explained by differences in the parameterizations of the saturation, sedimentation, and collection processes between the bin scheme and the MG scheme.

5.3 Relative importance of resolution and parameterizations

Comparisons between ARW simulations with different resolutions and those with different microphysics parameterizations as shown in Figures 3 and 13 demonstrate that the variation in cloud variables is much greater with respect to the variation in resolution than with the variation in microphysics parameterizations. For example, comparisons between Figures 3 and 13 show that the variation in the time- and domain-averaged cloud mass is ~2–4 times greater as resolution varies than when the microphysics parameterizations varies. These comparisons also show that the variation in cloud variables with varying resolution explains the discrepancy between the GFS simulations and the CSRM simulations and between the GFS simulations and observations much better than the variation in microphysics parameterizations. As a first step toward reducing the first-order errors in the GFS simulations, we first need to focus on the reduction in errors that are associated with the use of coarse resolution in the GFS model.

6. Summary and Discussion

This study examines the uncertainties in the simulations of clouds, precipitation, and CAPI in the NWP models. Here, we focus on those uncertainties that are created by the microphysics parameterizations and by the model resolution chosen. In particular, for the examination of the uncertainties associated with microphysics parameterizations, we investigate the contributions of the parameterizations of three key microphysical processes, i.e., saturation, collection, and sedimentation, to the uncertainties.

As a way of examining the uncertainties created by the microphysics parameterizations, we compare the MG scheme (a representative bulk scheme) to the bin scheme, which acts as a benchmark scheme. The vertical distribution of the cloud mass simulated by the MG scheme deviates substantially from that simulated by the bin scheme. In particular, there is a substantial discrepancy in the peak value of the distribution and the altitude of the peak value between the schemes. Also, there is a substantial discrepancy between the schemes in the sensitivity of the cloud mass to increasing aerosol concentrations.

The discrepancy in the sensitivity is closely linked to the discrepancy in the parameterization of the saturation processes between the schemes. The use of the saturation adjustment in the bulk scheme reduces the sensitivity by a factor of ~2 compared to the use of the supersaturation prediction in the bin scheme. The discrepancy in the peak value and its altitude between the schemes is strongly linked to the parameterization of sedimentation in the schemes. The use of identical parameterizations of saturation and sedimentation makes the sensitivity and the peak value and its altitude similar between the schemes, although there still remains a slight difference in the magnitude of the cloud mass. This remaining difference is explained by the discrepancy in the parameterization of the collection process. When the two schemes use identical parameterizations of the saturation, sedimentation, and collection processes, the sensitivity and the peak value and its altitude become nearly identical between the two schemes. This confirms that differences in the parameterizations of the three key processes (i.e., saturation, sedimentation, and collection) are the main cause of the differences in the simulations of clouds between the schemes as indicated by Fan et al. (2012) and Khain et al. (2015).

By selecting the simulations with the bin scheme as benchmark simulations, we see that the use of the saturation adjustment, as done in most current NWP models, can lead to an underestimation of the sensitivity of the cloud mass to increasing aerosol concentrations. Fan et al. (2012) and Khain et al. (2015) have also shown that the sensitivity of the cloud mass to increasing aerosol concentrations is lower in the bulk scheme than in the bin scheme. This study shows that the lower sensitivity in the bulk scheme is closely linked to the use of the saturation adjustment in the bulk scheme.

It is well known that the shape of the vertical profile of the cloud mass (i.e., the peak value of the cloud mass and its altitude) or how cloud mass is distributed in the vertical domain has substantial implications for cloud radiative forcing and precipitation processes. This study demonstrates that the different parameterizations of the sedimentation process between the schemes lead to different shapes of the cloud-mass profiles and thus different cloud radiative forcings and precipitation processes. The use of a mass-weight mean terminal velocity for sedimentation as done in the bulk schemes can lead to misleading shapes, cloud radiative forcings, and precipitation processes compared to those in the benchmark bin-scheme simulations where terminal velocities vary as hydrometeor sizes vary.

NWP models (e.g., the GFS model) adopt coarse resolution. This study shows that the use of coarse resolution can cause an underestimation of the updraft intensity and thus condensation and deposition, which leads to an underestimation of the cloud mass. Also, the use of coarse resolution likely results in the underestimation of the sensitivity of updrafts and cloud mass and that of evaporation, cloud system organization, and precipitation distributions to increasing aerosol concentrations.

Through the examination of the sensitivity of the results to resolution chosen, we find that updrafts, associated other cloud variables, and their sensitivity to increasing aerosol concentrations are strongly controlled by small-scale updrafts. When they are resolved with the use of high-resolution models, there are high-value averaged updrafts and associated variables, and their strong sensitivity but when they are not resolved in low-resolution models, there are low-value averaged updrafts and associated variables, and their weak sensitivity. This means that small-scale updrafts not resolved with coarse resolution play an important role in the simulation of the correct magnitude of updrafts, associated variables, and their sensitivity to increasing aerosol concentrations.

The frequency distributions of updrafts simulated in this study show that the frequency of weak updrafts is overestimated while that of strong updrafts is underestimated in the simulations with coarse resolution compared to those in the CSRM simulations. Hence, the updraft speed shifts toward lower values with coarsening resolution. The difference in the frequency between the polluted and clean scenarios reduces substantially, particularly for strong updrafts, with coarsening resolution. This is why the sensitivity of updrafts and associated cloud variables to increasing aerosol concentrations reduces with coarsening resolution. We see that not resolving small-scale updrafts results in the underestimation of strong updrafts and the overestimation of weak updrafts for both scenarios and in the reduced difference in strong updrafts between the scenarios.

The GFS simulations use the so-called sub-grid parameterizations (e.g., cumulus parameterizations) that represent sub-grid updrafts and associated variables, while the ARW simulations at the 500-m resolution (i.e., the CSRM simulations) do not use these sub-grid parameterizations based on consideration that the CSRM simulations resolve sub-grid processes. Thus, the CSRM simulations (that prove to act as benchmark simulations through comparisons to observations) are able to evaluate the sub-grid parameterizations in the GFS model. The sub-grid parameterizations are designed to correct errors that are caused by the use of coarse resolution in the GFS model. However, comparisons between the GFS simulations and the ARW simulations at different resolutions indicate that despite the presence of sub-grid parameterizations in the GFS model, the errors or differences in the updraft intensity and associated cloud variables between the GFS simulations and the CSRM simulations exist due to resolution. Hence, sub-grid parameterizations need to be improved to better represent sub-grid processes. To this end, results here indicate that sub-grid parameterizations (e.g., scale-aware cumulus schemes) which are being implemented into the NWP models (e.g., the GFS model) should be able to compensate for the over- and under-estimation of weak updrafts and strong updrafts, respectively, due to coarse resolution.

Comparisons between the GFS simulations and the ARW simulations also indicate that it is likely that the GFS model underestimates the sensitivity of updrafts and associated cloud variables to increasing aerosol concentrations. In general, parameterizations that represent sub-grid updrafts and other associated variables do not have pathways through which increasing aerosol concentrations affect updrafts and associated cloud variables. However, recent studies by Lim et al. (2014), Thayer-Calder et al. (2015), and Griffin and Larson (2016) have attempted to consider interactions among microphysical processes, their variations with varying aerosol concentrations, and sub-grid dynamic (e.g., updrafts and downdrafts) and thermodynamic (e.g., temperature) variables in those parameterizations. These efforts should focus on countering the variation in the sensitivity of updrafts, in particular strong updrafts and thus that of cloud variables, cloud system organization, and precipitation distributions to increasing aerosol concentrations with coarsening resolution. While the pattern of the sensitivity and its variation shown in this study provides valuable information useful for aiding these efforts, results may be different for different cloud types and environments, given the strong dependence of aerosol-cloud interactions on cloud type and environmental conditions. So to aid the efforts in a generalized way, future studies with more cases that involve various types of aerosol-cloud interactions are needed.

Acknowledgements. This study is supported by NOAA (Grant NOAA-NWS-NWSPO-2015-2004117), which also provided the GFS forecast data, and Korea Environmental Industry & Technology Institute funded by the Korea Ministry of Environment as "Climate Change Correspondence Program". This study is also supported by "Development of Climate and Atmospheric Environmental Applications" project, funded by ETRI, which is a subproject of "Development of Geostationary Meteorological Satellite Ground Segment (NMSC-2017-01)" program funded by NMSC of KMA.

References

Basu S, Z. N. Begum, E. N. Rajagopal, 1998, Impact of boundary-layer parameterization schemes on the prediction of the Asian summer monsoon. Boundary-Layer Meteorol. 86, 469–485.

Bogenschutz, P. A., and S. K. Krueger, 2013, A simplified PDF parameterization of subgrid-scale clouds and turbulence for cloud-resolving models, J. Adv. Model. Earth Syst., 5, 195–211, doi:10.1002/jame.20018.

Donelan, M. A., B. K. Haus, N. Reul, et al., 2004, On the limiting aerodynamic roughness of the ocean in very strong winds. Geophys. Res. Lett., 31, doi: 10.1029/2004GL019460.

Griffin, B. M. and V. E. Larson, 2016, Parameterizing microphysical effects on variances and covariances of moisture and heat content using a multivariate probability density function: a study with CLUBB (tag MVCS), Geosci. Model Dev., 9, 4273-4295, doi:10.5194/gmd-9-4273-2016.

Hwang, S.-O., and D.-K. Lee, 1993, A study on the relationship between heavy rainfalls and associated low-level jets in the Korean peninsula, J. Korean Meteorol. Soc., 29, 133–146.

Fan J, T. Yuan, J. M. Comstock, et al., 2009. Dominant role by vertical wind shear in regulating aerosol effects on deep convective clouds." J. Geophys. Res., 114, doi:10.1029/2009JD012352.

Fan, J., L. R. Leung, Z. Li, H. Morrison, et al., 2012, Aerosol impacts on clouds and precipitation in eastern China: Results from bin and bulk microphysics, J. Geophys. Res., 117, D00K36, doi:10.1029/2011JD016537.

Fan, J., L.R. Leung, D. Rosenfeld, Q. Chen, Z. Li, J. Zhang, H. Yan, 2013, Microphysical effect determine macrophysical response for aerosol impact on deep convective clouds, Proceedings of National Academy of Sciences (PNAS), doi:10.1073/pnas.1316830110.

Fouquart, Y., and B. Bonnel, B., 1980, Computations of solar heating of the Earth's atmosphere: A new parameterization, Beitr. Phys. Atmos., 53, 35-62.

Khain, A. P., D. Rosenfeld, and A. Pokrovsky, 2005, Aerosol impact on the dynamics and microphysics of deep convective clouds, Q. J. R. Meteorol. Soc., 131, 2639–2663, doi:10.1256/qj.04.62.

Khain, A., and B. Lynn, 2009, Simulation of a supercell storm in clean and dirty atmosphere using weather research and forecast model with spectral bin microphysics, J. Geophys. Res., 114, D19209, doi:10.1029/2009JD011827.

Khain, A. P., et al., 2015, Representation of microphysical processes in cloudresolving models: Spectral (bin) microphysics versus bulk parameterization, Rev. Geophys., 53, 247–322, doi:10.1002/2014RG000468.

Kim, J. H., S. S. Yum, S. Shim, et al., 2014, On the submicron aerosol distributions and CCN number concentrations in and around the Korean Peninsula, Atmos. Chem. Phys., 14, 8763-8779, doi:10.5194/acp-14-8763-2014.

Lance, S., A. Nenes, C. Mazzoleni, et. al., 2009, Cloud condensation nuclei activity, closure, and droplet growth kinetics of Houston aerosol during the Gulf of Mexico Atmospheric Composition and Climate Study (GoMACCS), J. Geophys. Res., 114, D00F15,

doi:10.1029/2008JD011699.
Lee, S. S. and G. Feingold, 2013, Aerosol effects on the cloud-field properties of tropical convective clouds, Atmos. Chem. Phys., 13, 6713-6726.
Lee, S. S., W.-K. Tao, and C. H. Jung, 2014, Aerosol effects on instability, circulations, clouds and precipitation, Advances in Meteorology, Article ID 683950.
Lee, S. S., Z. Li, J. Mok, et al., 2017, Interactions between aerosol absorption, thermodynamics, dynamics, and microphysics and their impacts on a multiple-cloud system, Clim. Dynam., doi: 10.1007/s00382-017-3552-x.
Li, Z., F. Niu, J. Fan, Y. Liu, D. Rosenfeld, and Y. Ding, 2011, Long-term impacts of aerosols on the vertical development of clouds and precipitation, Nature Geo., doi: 10.1038/NGEO1313.
Lim, K. S., J. Fan, L. Y. R. Leung, et al., 2014, Investigation of aerosol indirect effects using a cumulus microphysics parameterization in a regional climate model, J. Geophys. Res., 119, 906-926.
Mlawer, E. J., S. J. Taubman, P. D. Brown, M. J. Iacono, and S. A. Clough, 1997, RRTM, a validated correlated-k model for the longwave, J. Geophys. Res., 102, 16663-16682.
Moorthi, S., H.-L. Pan, and P. Caplan, Changes to the 2001 NCEP operational MRF/AVN global analysis/forecast system, 2001, Technical Procedures Bulletin, 484, 14pp., obtainable at http://www.nws.noaa.gov/om/tpb/484.htm
Morcrette, J.-J., A. Benedetti, A. Ghelli, J.W. Kaiser, A.M. Tompkins, 2011, Aerosol-cloud-radiation interactions and their Impact on ECMWF/MACC forecasts, Technical Memorandum, 660, 35pp.
Morrison, H., and A. Gettelman, 2008: A new two-moment bulk stratiform cloud microphysics scheme in the Community Atmosphere Model, version 3 (CAM3). Part I: Description and numerical tests, J. Climate, 21, 3642--3659, doi10.1175/2008JCLI2105.1.
Morrison, H., G. Thompson, and V. Tatarskii, 2009, Impact of cloud microphysics on the development of trailing stratiform precipitation in a simulated squall line: Comparison of one- and two-moment schemes, Mon. Wea. Rev., 137, 991–1007.
Pan, H.-L., and W.-S. Wu, 1995, Implementing a mass flux convective parameterization package for the NMC Medium-Range Forecast model, NMC Office Note 409, 40 pp.
Randall, D. A., M. E. Schlesinger, V. Galin, V. Meleshko, J.-J. Morcrette, and R. Wetherald, 2006, Cloud Feedbacks. In "Frontiers in the Science of Climate Modeling," J. T. Kiehl and V. Ramanathan, Eds., Cambridge University Press, 217-250.
Seifert, A., and D. Beheng, 2006, A two-moment cloud microphysics parameterization for mixed-phase clouds. Part 2: Maritime vs. continental deep convective storms, Meteorol. Atmos. Phys., 92, 67-82.
Seifert, A., C. Köhler, and K. D. Beheng, Aerosol-cloud-precipitation effects over Germany as simulated by a convective-scale numerical weather prediction model, Atmos. Chem. Phys., 12, 709-725, doi:10.5194/acp-12-709-2012, 2012.
Storer, R.L., S.C. van den Heever, and G.L. Stephens, 2010, Modeling aerosol impacts on convective storms in different environments, J. Atmos. Sci., 67, 3904-3915.
Sudhakar, D., J. Quaas, R. Wolke, J. Stoll, A. Mühlbauer, M. Salzmann, B. Heinold, and I. Tegen, 2016, Implementation of aerosol-cloud interactions in the regional atmosphere-aerosol model

COSMO-MUSCAT and evaluation using satellite data, Geosci. Model Dev. Discuss., doi:10.5194/gmd-2016-186.

Sun, J., T.-Y. Lee, 2002, A numerical study of an intense quasistationary convection band over the Korean peninsula, J. Meteorol. Soc. Jpn., 80, 1221–1245.

Sundqvist, H., E. Berge, and J. E. Kristjansson, 1989, Condensation and cloud parameterization studies with a mesoscale numerical weather prediction model, Mon. Weather Rev., 117, 1641-1657.

Tao, W.-K., X. Li, A. Khain, T. Matsui, S. Lang, and J. Simpson, 2007, The role of atmospheric aerosol concentration on deep convective precipitation: cloud-resolving model simulations, J. Geophys. Res., 112, D24S18, doi:10.1029/2007JD008728.

Tao, W.-K., J. P. Chen, Z. Li, and C. Zhang, 2012, Impact of aerosols on convective clouds and precipitation, Rev. of Geophy., 50, RG2001, doi:10.1029/2011RG000369.

Thayer-Calder, K., A. Gettelman, C. Craig, et al., 2015, A unified parameterization of clouds and turbulence using CLUBB and subcolumns in the Community Atmosphere Model, Geosci. Model Dev., 8, 3801-3821, doi:10.5194/gmd-8-3801-2015.

van den Heever, S.C., and W.R. Cotton, 2007, Urban aerosol impacts on downwind convective storms, J. Appl. Meteor. Climatol., 46, 828-850.

van den Heever, S. C., G. L. Stephens, and N. B. Wood, 2011, Aerosol indirect effects on tropical convection characteristics under conditions of radiative-convective equilibrium, J. Atmos. Sci., 68, 699-718.

Wang, H., W. C. Skamarock, and G. Feingold, 2009, Evaluation of scalar advection schemes in the Advanced Research WRF model using large-eddy simulations of aerosol-cloud interactions, Mon. Wea. Rev., 137, 2547-2558.

Zeng, X., and A. Beljaars, 2005, A prognostic scheme of sea surface skin temperature for modeling and data assimilation, Geophys. Res. Lett, 32, L14605, doi:10.1029/2005GL023030, 2005.

Zhao, Q. Y., and F. H. Carr, 1997, A prognostic cloud scheme for operational NWP models, Mon. Wea. Rev., 125, 1931- 1953.

Tables

Table 1. Description of the simulations.

Simulations	Case	Aerosol number concentration at the surface (cm^{-3})	Microphysics scheme	Resolution	Saturation	Sedimentation	Collection
High-aerosol-Seoul run	Seoul	5500	Bin	500 m	Supersaturation prediction	Bin-scheme sedimentation	Bin-scheme collection
Low-aerosol-Seoul run	Seoul	550	Bin	500 m	Supersaturation prediction	Bin-scheme sedimentation	Bin-scheme collection
High-aerosol-Houston run	Houston	1500	Bin	500 m	Supersaturation prediction	Bin-scheme sedimentation	Bin-scheme collection
Low-aerosol-Houston run	Houston	150	Bin	500 m	Supersaturation prediction	Bin-scheme sedimentation	Bin-scheme collection
High-aerosol-15-Seoul run	Seoul	5500	Bin	15 km	Supersaturation prediction	Bin-scheme sedimentation	Bin-scheme collection
Low-aerosol-15-Seoul run	Seoul	550	Bin	15 km	Supersaturation prediction	Bin-scheme sedimentation	Bin-scheme collection
High-aerosol-15-Houston run	Houston	1500	Bin	15 km	Supersaturation prediction	Bin-scheme sedimentation	Bin-scheme collection
Low-aerosol-15-Houston	Houston	150	Bin	15 km	Supersaturation prediction	Bin-scheme sedimentation	Bin-scheme collection

run							
High-areosol-35-Seoul run	Seoul	5500	Bin	35 km	Supersaturation prediction	Bin-scheme sedimentation	Bin-scheme collection
Low-aerosol-35-Seoul run	Seoul	550	Bin	35 km	Supersaturation prediction	Bin-scheme sedimentation	Bin-scheme collection
High-aerosol-35-Houston run	Houston	1500	Bin	35 km	Supersaturation prediction	Bin-scheme sedimentation	Bin-scheme collection
Low-aerosol-35-Houston run	Houston	150	Bin	35 km	Supersaturation prediction	MG-scheme sedimentation	MG-scheme collection
High-aerosol-MG-Seoul run	Seoul	5500	MG	500 m	Saturation adjustment	MG-scheme sedimentation	MG-scheme collection
Low-aerosol-MG-Seoul run	Seoul	550	MG	500 m	Saturation adjustment	MG-scheme sedimentation	MG-scheme collection
High-aerosol-MG-Houston run	Houston	1500	MG	500 m	Saturation adjustment	MG-scheme sedimentation	MG-scheme collection
Low-aerosol-MG-Houston run	Houston	150	MG	500 m	Saturation adjustment	MG-scheme sedimentation	MG-scheme collection
High-aerosol-sat-Seoul run	Seoul	5500	Bin	500 m	Saturation adjustment	Bin-scheme sedimentation	Bin-scheme collection
Low-aerosol-sat-Seoul run	Seoul	550	Bin	500 m	Saturation adjustment	Bin-scheme sedimentation	Bin-scheme collection
High-aerosol-	Houston	1500	Bin	500 m	Saturation	Bin-scheme	Bin-scheme

sat-Houston run					adjustment	sedimentation	collection
Low-aerosol-sat-Houston run	Houston	150	Bin	500 m	Saturation adjustment	Bin-scheme sedimentation	Bin-scheme collection
High-aerosol-sed-Seoul run	Seoul	5500	Bin	500 m	Saturation adjustment	MG-scheme sedimentation	Bin-scheme collection
Low-aerosol-sed-Seoul run	Seoul	550	Bin	500 m	Saturation adjustment	MG-scheme sedimentation	Bin-scheme collection
High-aerosol-sed-Houston run	Houston	1500	Bin	500 m	Saturation adjustment	MG-scheme sedimentation	Bin-scheme collection
Low-aerosol-sed-Houston run	Houston	150	Bin	500 m	Saturation adjustment	MG-scheme sedimentation	Bin-scheme collection
High-aerosol-col-Seoul run	Seoul	5500	Bin	500 m	Saturation adjustment	MG-scheme sedimentation	MG-scheme collection
Low-aerosol-col-Seoul run	Seoul	550	Bin	500 m	Saturation adjustment	MG-scheme sedimentation	MG-scheme collection
High-aerosol-col-Houston run	Houston	1500	Bin	500 m	Saturation adjustment	MG-scheme sedimentation	MG-scheme collection
Low-aerosol-col-Houston run	Houston	150	Bin	500 m	Saturation adjustment	MG-scheme sedimentation	MG-scheme collection

FIGURE CAPTIONS

Figure 1. (a) Sea-level pressure (hPa) and (b) 850 hPa wind (m s^{-1}; arrows), geopotential height (m; contours) and equivalent potential temperature (K; shaded) at 0900 LST July 26th 2011 over the northeast Asia. The rectangles in the Korean Peninsula in panels (a) and (b) mark the center of Seoul. (c) Sea-level pressure (hPa;shaded) and wind at 10 m above sea level (m s^{-1}; barbs) and (d) convective available potential energy (J kg^{-1}) at 0500 LST 18 July 2013 in and around Houston. The rectangles in panels (c) and (d) mark the center of Houston.

Figure 2. (a) The domain (marked by the rectangle) used in simulations for the Seoul case. The small white circle marks the center of Seoul. (b) The domain used in simulations for the Houston case. The small white circle marks the center of Houston.

Figure 3. Vertical distributions of the time- and domain-averaged cloud liquid content (CLC) for (a) the Seoul case and (b) the Houston case. Solid lines represent simulations at the 500-m resolution, while dashed lines represent those at the 15-km resolution. Dotted lines represent simulations at the 35-km resolution and blue lines represent GFS-simulated CLC.

Figure 4. Same as Figure 3, but for cloud ice content (CIC).

Figure 5. Time series of the domain-averaged (a) liquid water path (LWP) and (b) ice water path (IWP) for the Seoul case. Solid lines represent simulations at the 500-m resolution, while dashed and dotted lines represent those at 15- and 35-km resolutions, respectively. Blue lines represent GFS-simulated LWP and IWP and green lines represent observed LWP and IWP.

Figure 6. Same as Figure 5, but for the Houston case.

Figure 7. Vertical distributions of the time- and domain-averaged updraft mass fluxes for (a) the Seoul case and (b) the Houston case. Solid lines represent simulations at the 500-m resolution, while dashed lines represent those at the 15-km resolution. Dotted lines represent simulations at the 35-km resolution and blue lines represent GFS-simulated updraft mass fluxes.

Figure 8. Vertical distributions of the time- and domain-averaged condensation rates for (a) the Seoul case and (b) the Houston case. Solid lines represent simulations at the 500-m resolution, while dashed lines represent those at the 15-km resolution. Dotted lines represent simulations at the 35-km resolution.

Figure 9. Same as Figure 8, but for deposition rates.

Figure 10. Distributions of normalized updraft frequency over updraft speeds for (a) the Seoul case and (b) the Houston case. Solid lines represent simulations at the 500-m resolution, while dashed lines represent those at the 15-km resolution. Dotted lines represent simulations at the 35-km resolution.

Figure 11. Same as Figure 8, but for evaporation rates.

Figure 12. Distributions of normalized precipitation frequency over precipitation rates for (a) the Seoul case and (b) the Houston case. Solid lines represent simulations at the 500-m resolution, while dashed lines represent those at the 15-km resolution. Dotted lines represent simulations at the 35-km resolution.

Figure 13. Vertical distributions of the time- and domain-averaged cloud liquid content (CLC) for (a) the Seoul case and (b) the Houston case. Solid red and black lines represent simulations with the bin scheme and at the 500-m resolution, while dashed red and black lines represent the bin-scheme simulations with the saturation adjustment. Solid yellow and green lines represent simulations with the MG scheme.

Figure 14. Vertical distributions of the time- and domain-averaged cloud liquid content (CLC) for (a) the Seoul case and (b) the Houston case. Solid red and black lines represent simulations with the bin scheme and at the 500-m resolution, while dashed red and black lines represent the bin-scheme

simulations with the saturation adjustment and the MG scheme sedimentation process. Solid yellow and green lines represent simulations with the MG scheme.

Figure 15. Vertical distributions of the time- and domain-averaged cloud liquid content (CLC) for (a) the Seoul case and (b) the Houston case. Solid red and black lines represent simulations with the bin scheme and at the 500-m resolution, while dashed red and black lines represent the bin-scheme simulations with the saturation adjustment and the MG scheme sedimentation and collection processes. Solid yellow and green lines represent simulations with the MG scheme.

a

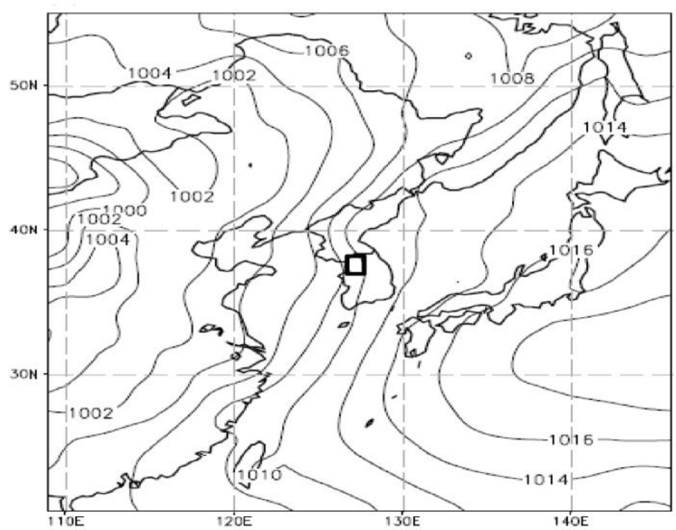
1004
1002
1006
1008
1014
1002
1000
1002
1004
1016
1002
1016
1010
1014
50N
40N
30N
110E
120E
130E
140E

b

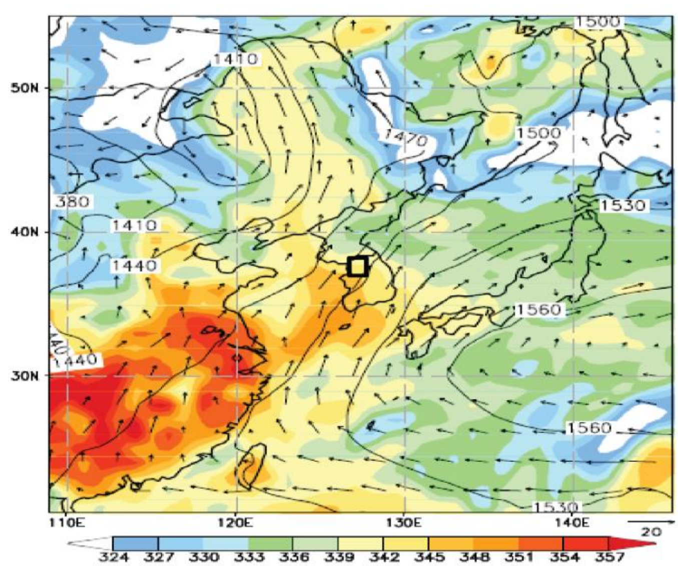
1500
1410
1470
1500
1380
1530
1410
1440
1560
1440
1560
1530
50N
40N
30N
110E
120E
130E
140E
20
324 327 330 333 336 339 342 345 348 351 354 357

Figure 1

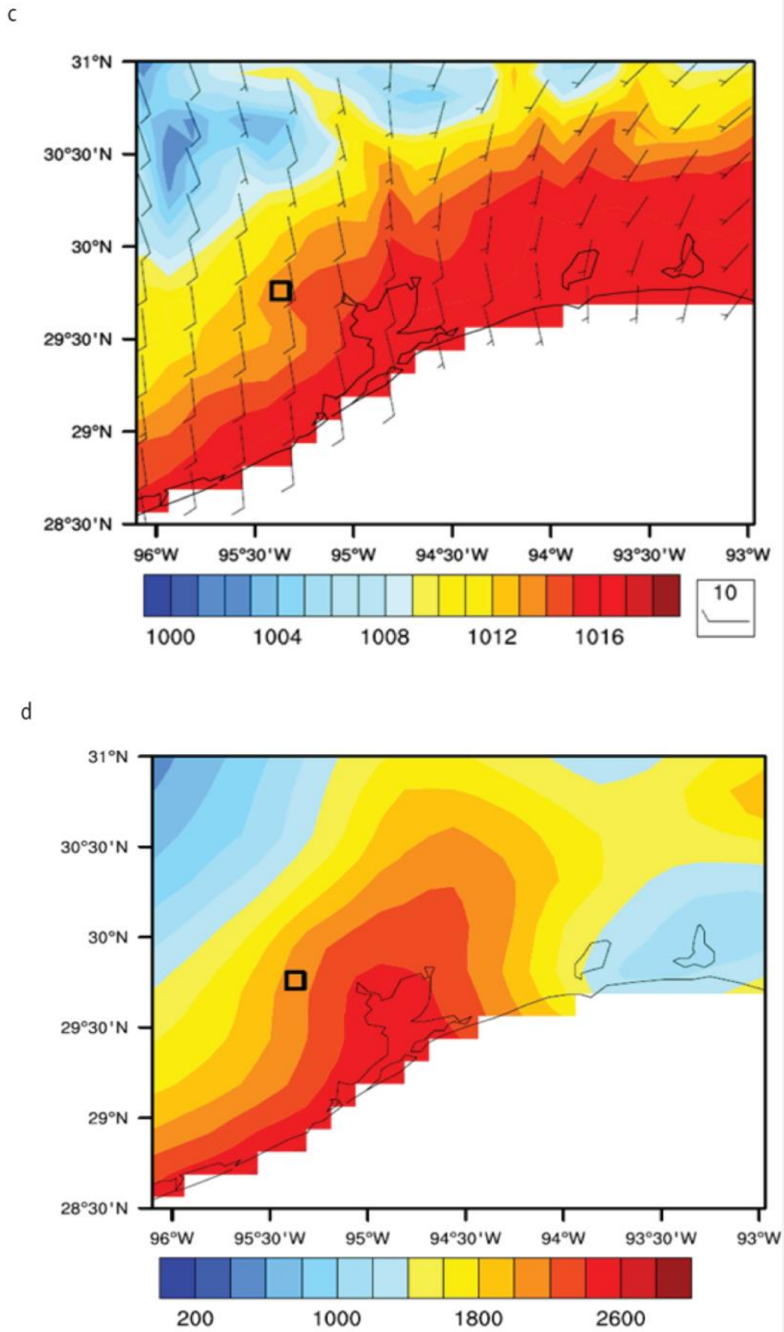
c
31°N
30°30'N
30°N
29°30'N
29°N
28°30'N
96°W
95°30'W
95°W
94°30'W
94°W
93°30'W
93°W
1000
1004
1008
1012
1016
10
d
31°N
30°30'N
30°N
29°30'N
29°N
28°30'N
96°W
95°30'W
95°W
94°30'W
94°W
93°30'W
93°W
200
1000
1800
2600

Figure 1

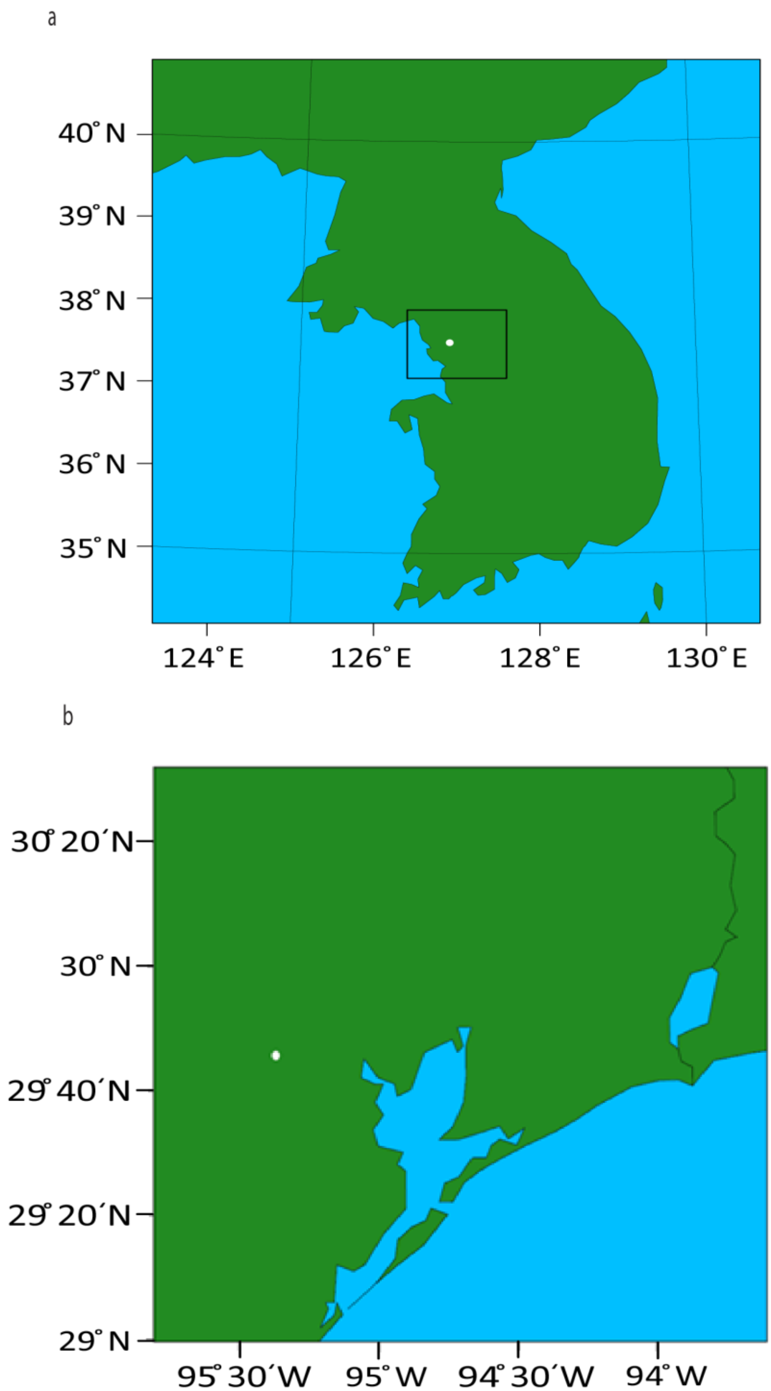
a
40° N
39° N
38° N
37° N
36° N
35° N
124° E
126° E
128° E
130° E
b
30° 20′ N
30° N
29° 40′ N
29° 20′ N
29° N
95° 30′ W
95° W
94° 30′ W
94° W

Figure 2

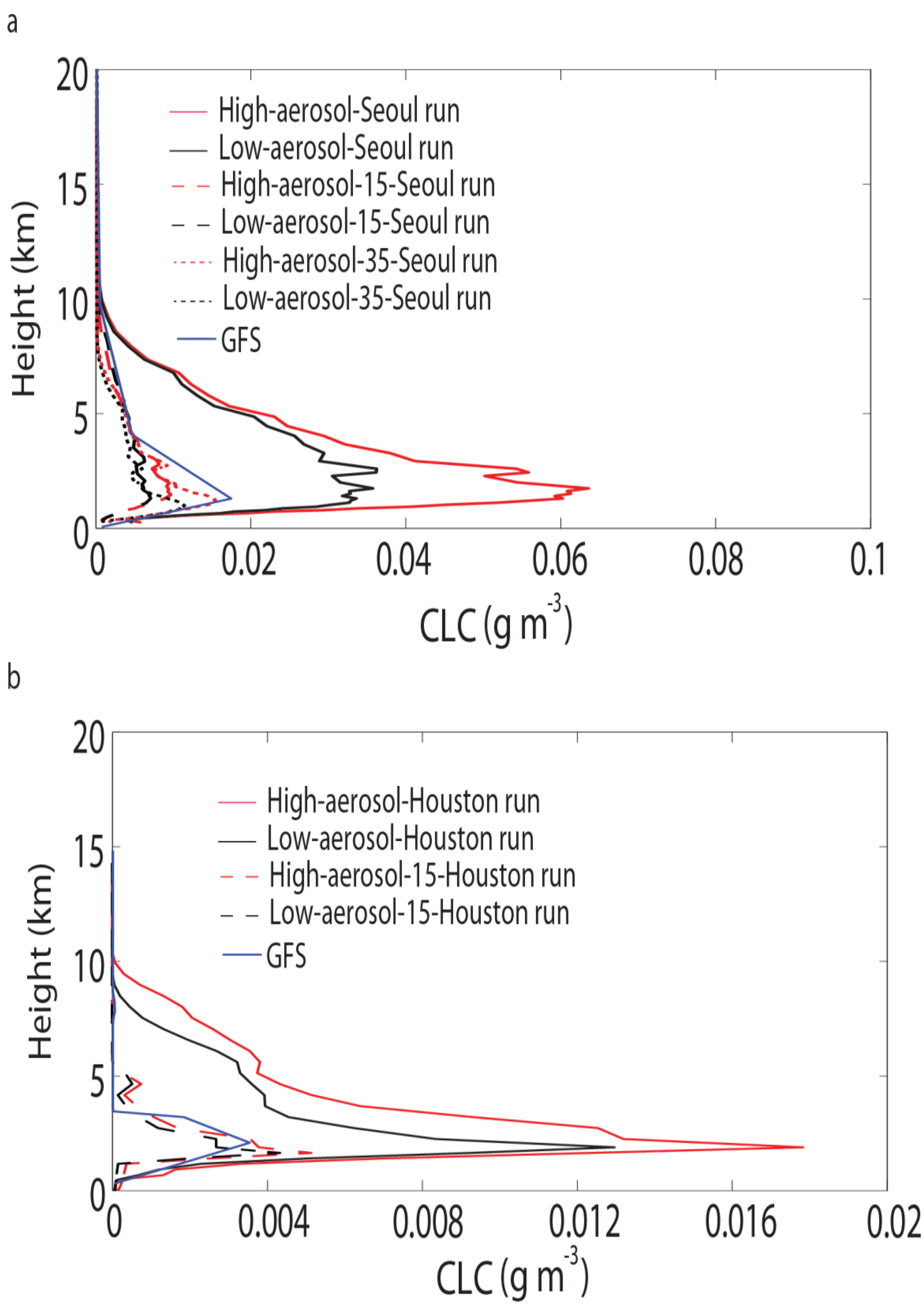
a
High-aerosol-Seoul run
Low-aerosol-Seoul run
High-aerosol-15-Seoul run
Low-aerosol-15-Seoul run
High-aerosol-35-Seoul run
Low-aerosol-35-Seoul run
GFS
Height (km)
CLC (g m-3)
b
High-aerosol-Houston run
Low-aerosol-Houston run
High-aerosol-15-Houston run
Low-aerosol-15-Houston run
GFS
Height (km)
CLC (g m-3)

Figure 3

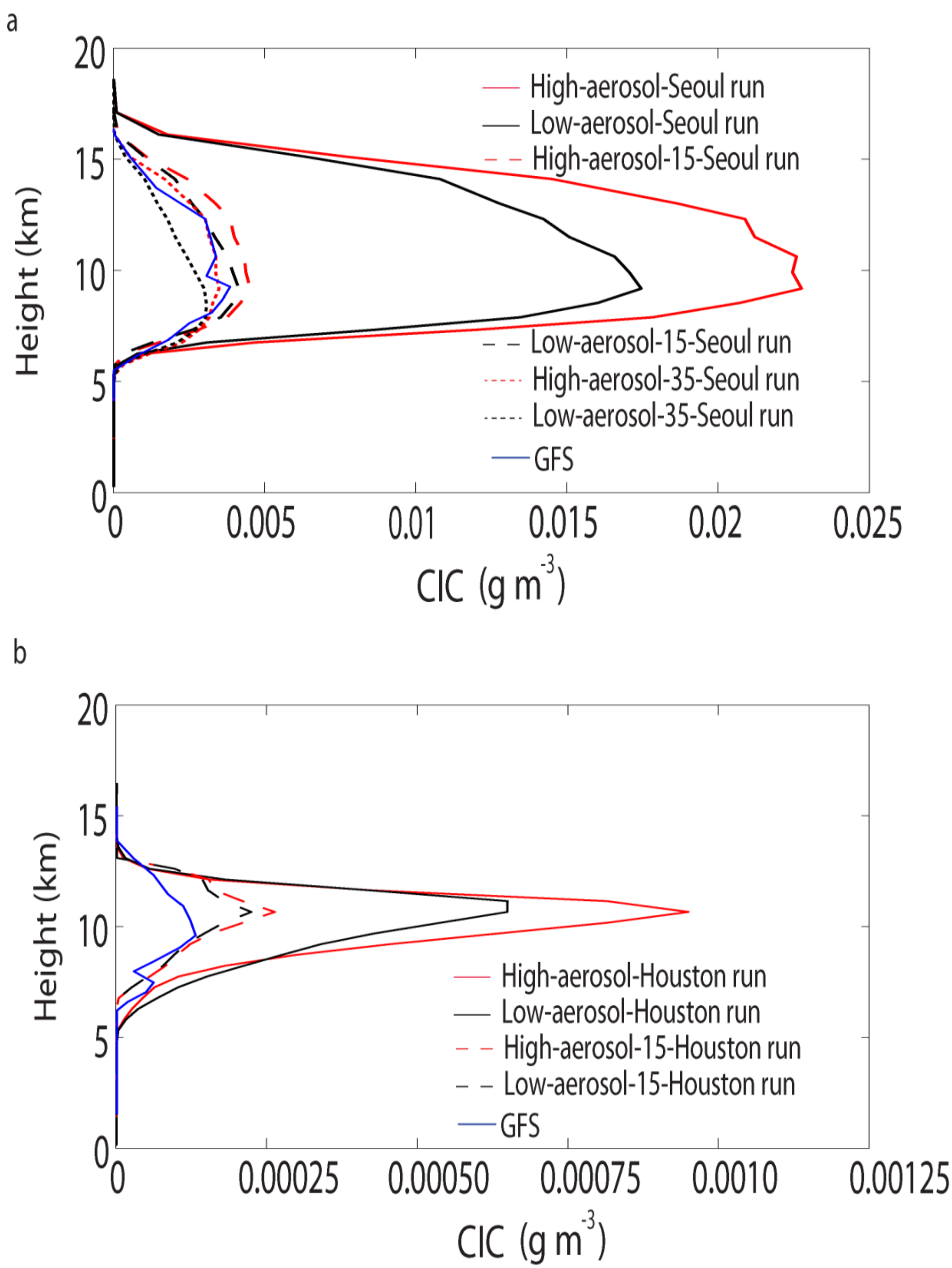
a
High-aerosol-Seoul run
Low-aerosol-Seoul run
High-aerosol-15-Seoul run
Low-aerosol-15-Seoul run
High-aerosol-35-Seoul run
Low-aerosol-35-Seoul run
GFS
Height (km)
0
5
10
15
20
0
0.005
0.01
0.015
0.02
0.025
CIC (g m-3)
b
High-aerosol-Houston run
Low-aerosol-Houston run
High-aerosol-15-Houston run
Low-aerosol-15-Houston run
GFS
Height (km)
0
5
10
15
20
0
0.00025
0.00050
0.00075
0.0010
0.00125
CIC (g m-3)

Figure 4

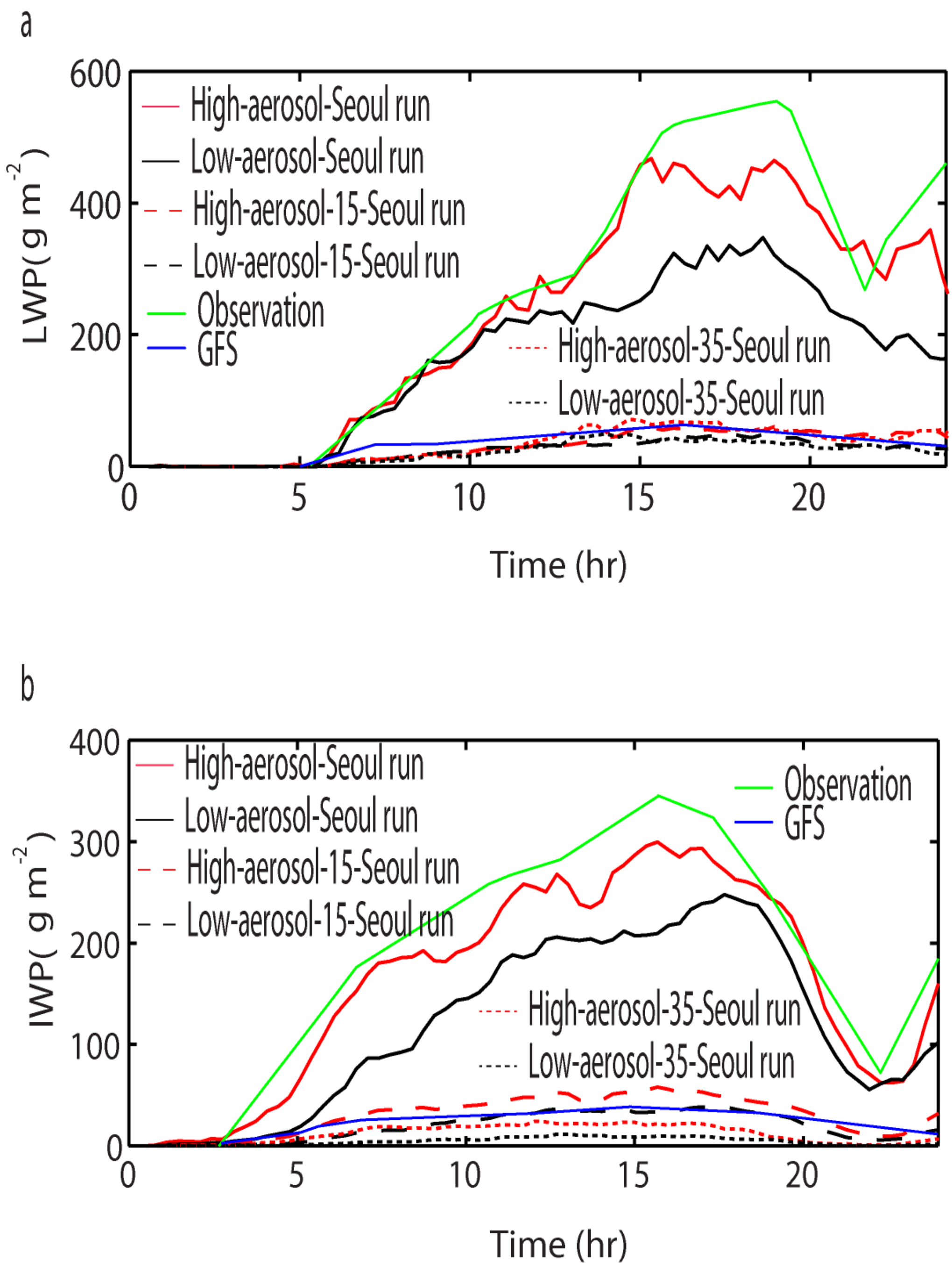
a
High-aerosol-Seoul run
Low-aerosol-Seoul run
High-aerosol-15-Seoul run
Low-aerosol-15-Seoul run
Observation
GFS
High-aerosol-35-Seoul run
Low-aerosol-35-Seoul run
LWP(g m-2)
Time (hr)
b
High-aerosol-Seoul run
Low-aerosol-Seoul run
High-aerosol-15-Seoul run
Low-aerosol-15-Seoul run
Observation
GFS
High-aerosol-35-Seoul run
Low-aerosol-35-Seoul run
IWP(g m-2)
Time (hr)

Figure 5

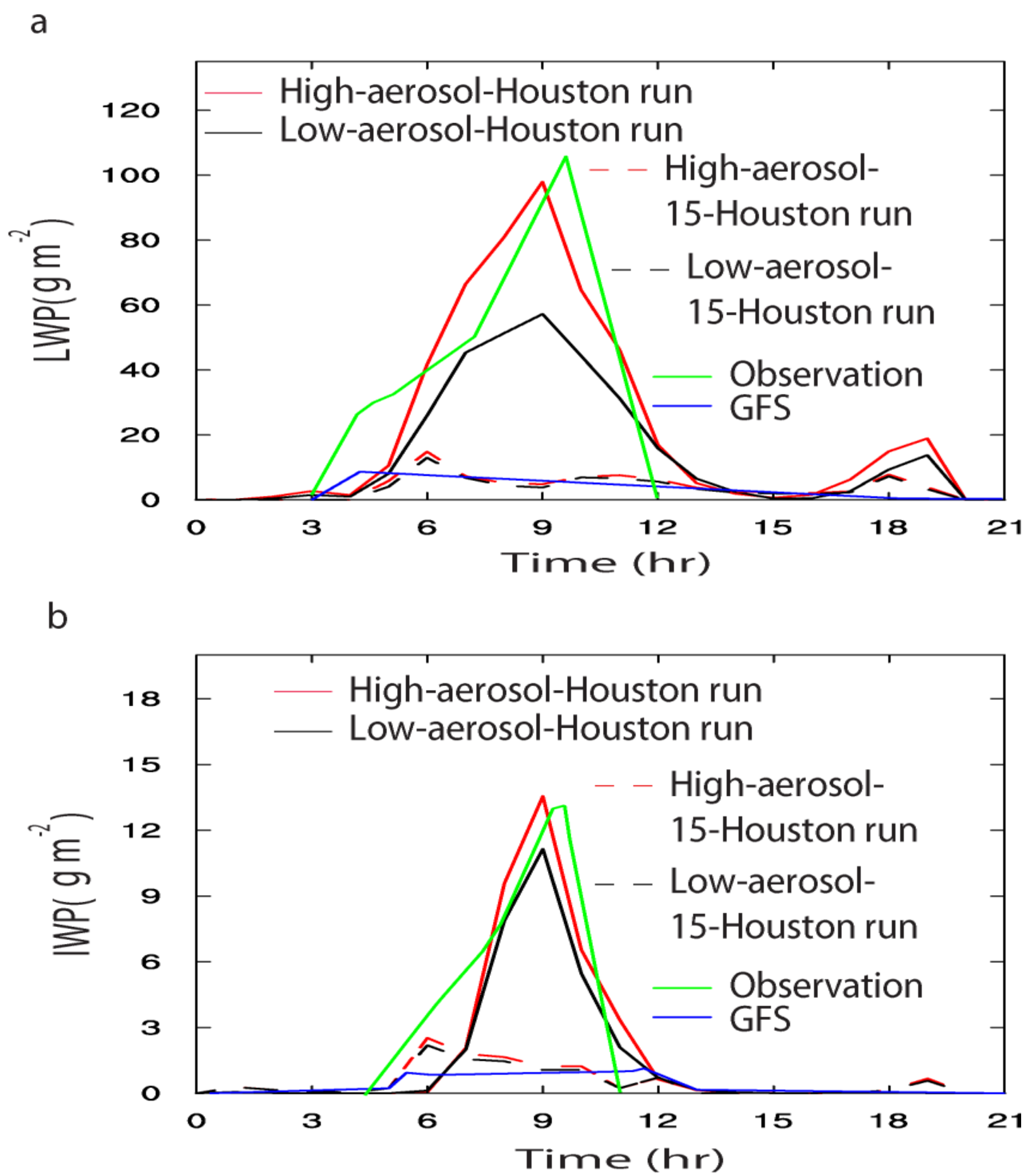
a
High-aerosol-Houston run
Low-aerosol-Houston run
High-aerosol-15-Houston run
Low-aerosol-15-Houston run
Observation
GFS
LWP(g m-2)
Time (hr)
b
High-aerosol-Houston run
Low-aerosol-Houston run
High-aerosol-15-Houston run
Low-aerosol-15-Houston run
Observation
GFS
IWP(g m-2)
Time (hr)

Figure 6

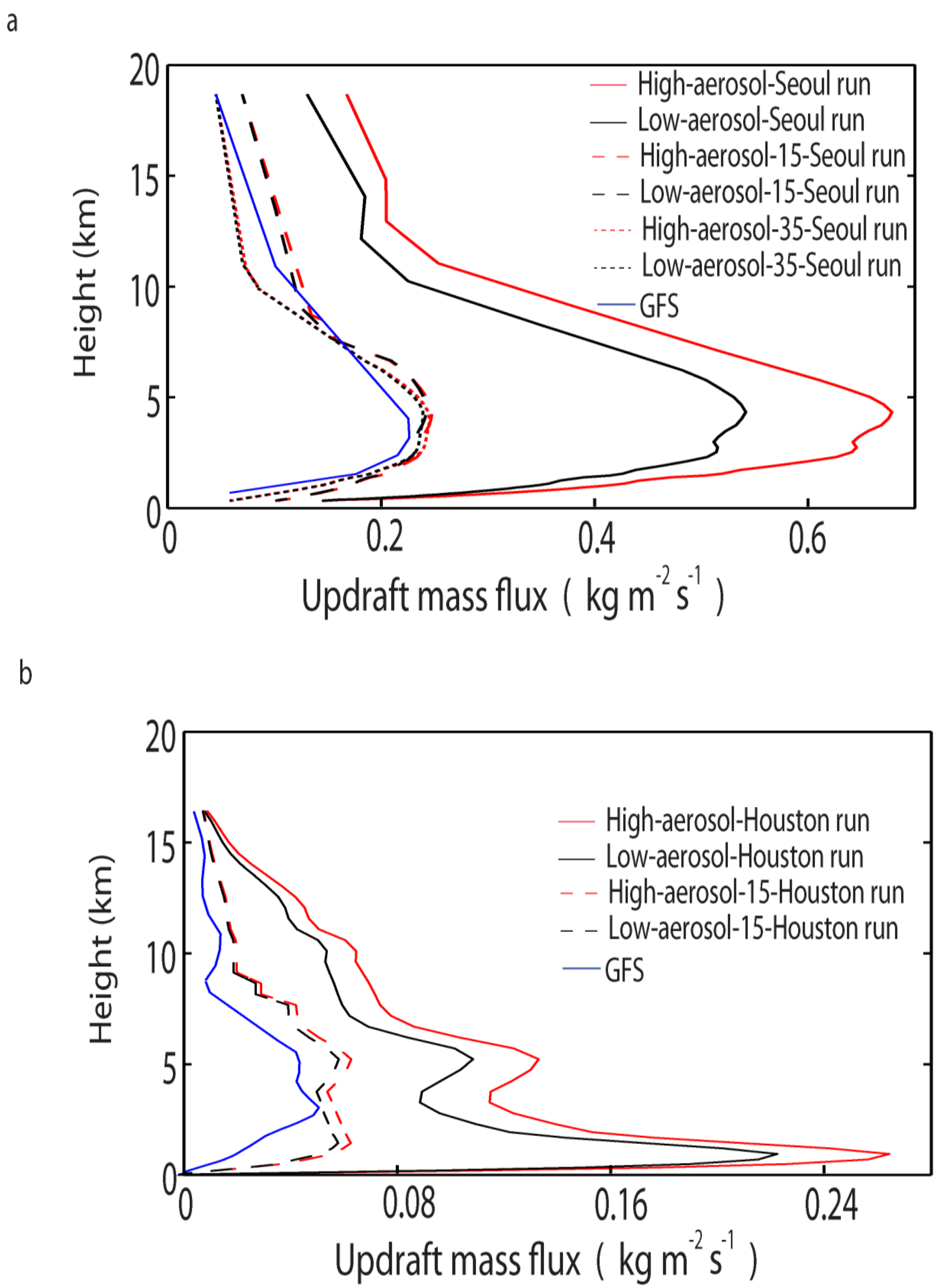
a
High-aerosol-Seoul run
Low-aerosol-Seoul run
High-aerosol-15-Seoul run
Low-aerosol-15-Seoul run
High-aerosol-35-Seoul run
Low-aerosol-35-Seoul run
GFS
Height (km)
0
5
10
15
20
0
0.2
0.4
0.6
Updraft mass flux (kg m^{-2} s^{-1})
b
High-aerosol-Houston run
Low-aerosol-Houston run
High-aerosol-15-Houston run
Low-aerosol-15-Houston run
GFS
Height (km)
0
5
10
15
20
0
0.08
0.16
0.24
Updraft mass flux (kg m^{-2} s^{-1})

Figure 7

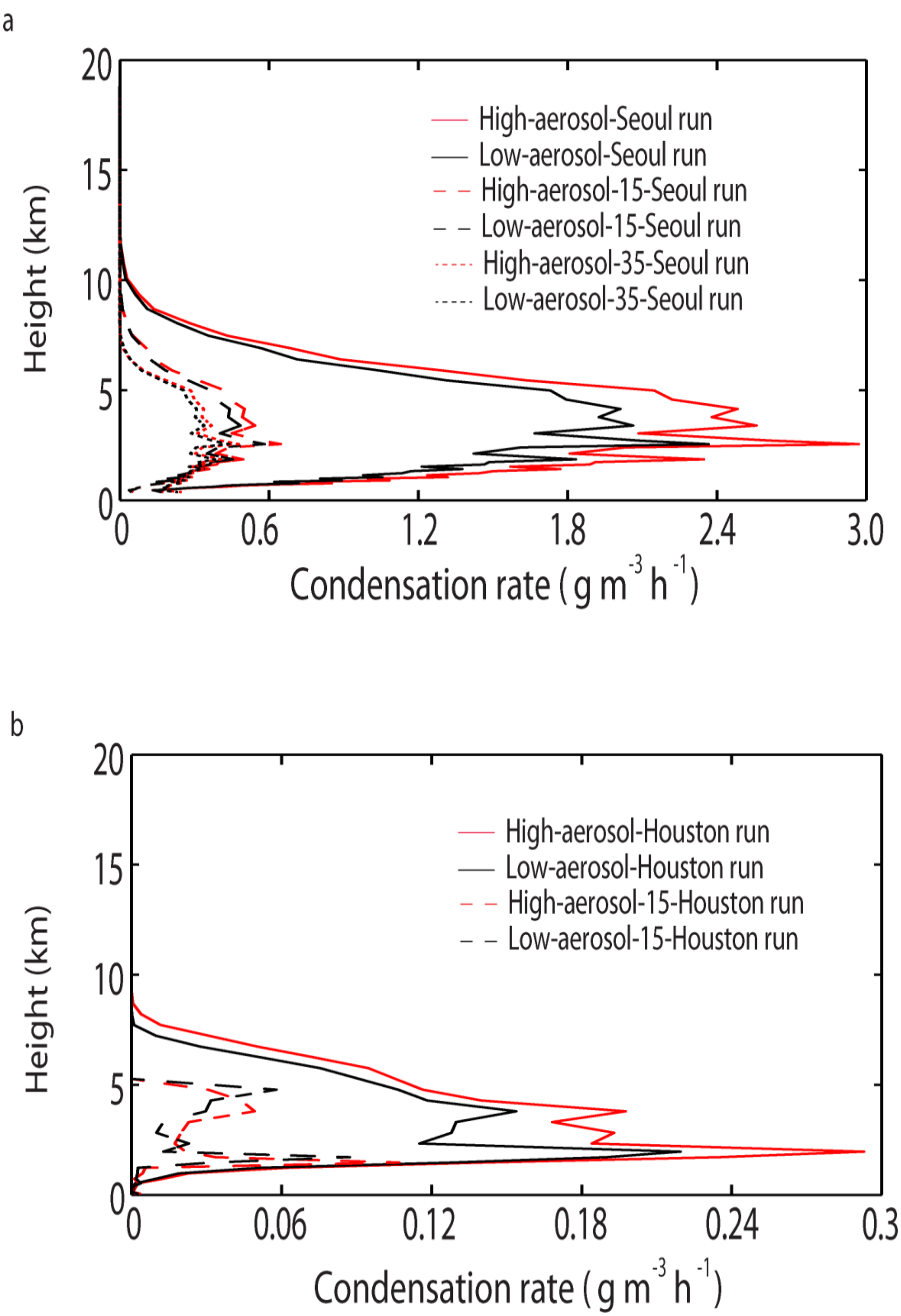
a
High-aerosol-Seoul run
Low-aerosol-Seoul run
High-aerosol-15-Seoul run
Low-aerosol-15-Seoul run
High-aerosol-35-Seoul run
Low-aerosol-35-Seoul run
Height (km)
0
5
10
15
20
0
0.6
1.2
1.8
2.4
3.0
Condensation rate (g m^{-3} h^{-1})
b
High-aerosol-Houston run
Low-aerosol-Houston run
High-aerosol-15-Houston run
Low-aerosol-15-Houston run
Height (km)
0
5
10
15
20
0
0.06
0.12
0.18
0.24
0.3
Condensation rate (g m^{-3} h^{-1})

Figure 8

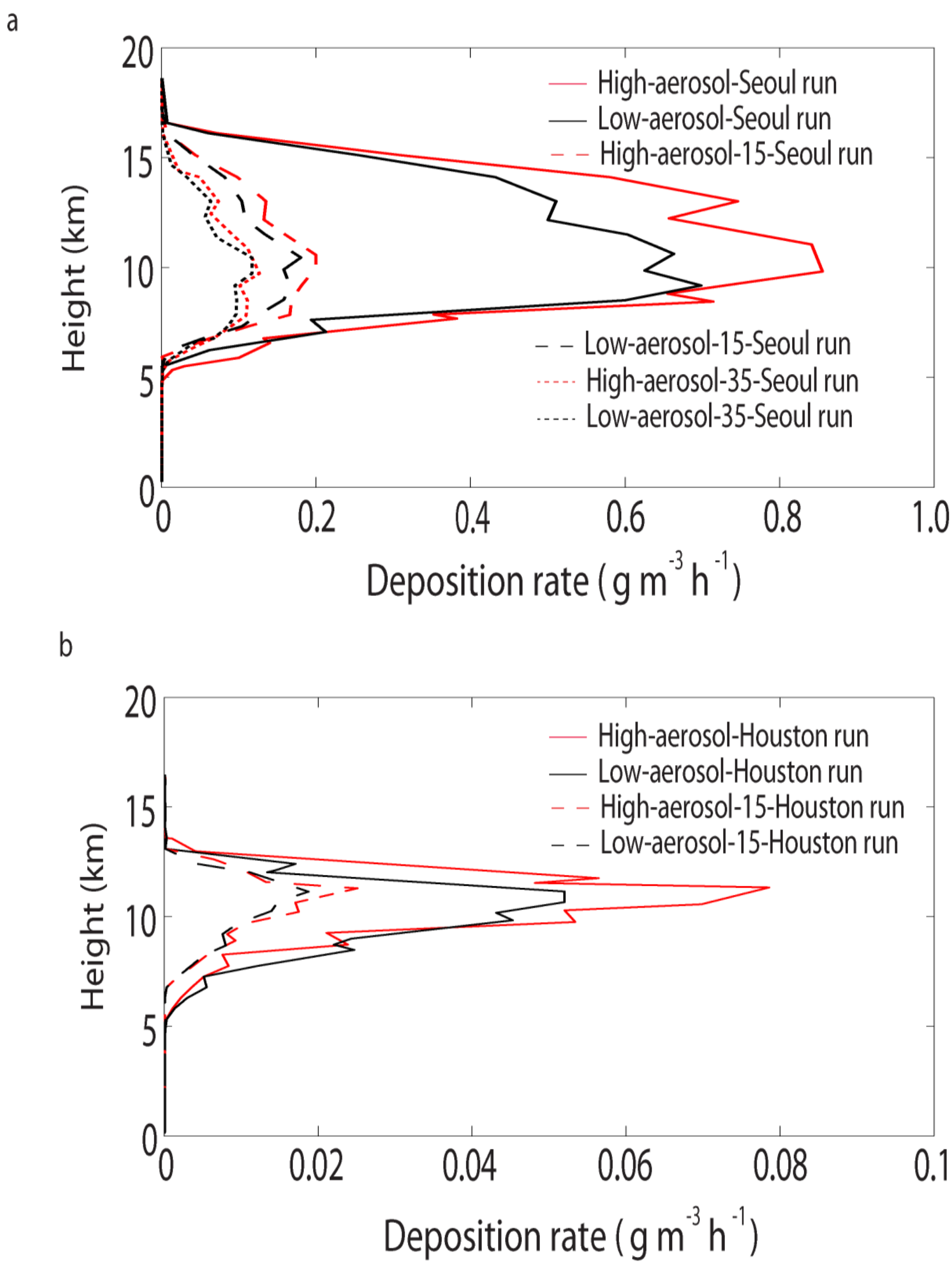
a
High-aerosol-Seoul run
Low-aerosol-Seoul run
High-aerosol-15-Seoul run
Low-aerosol-15-Seoul run
High-aerosol-35-Seoul run
Low-aerosol-35-Seoul run
Height (km)
Deposition rate (g m^{-3} h^{-1})
b
High-aerosol-Houston run
Low-aerosol-Houston run
High-aerosol-15-Houston run
Low-aerosol-15-Houston run
Height (km)
Deposition rate (g m^{-3} h^{-1})

Figure 9

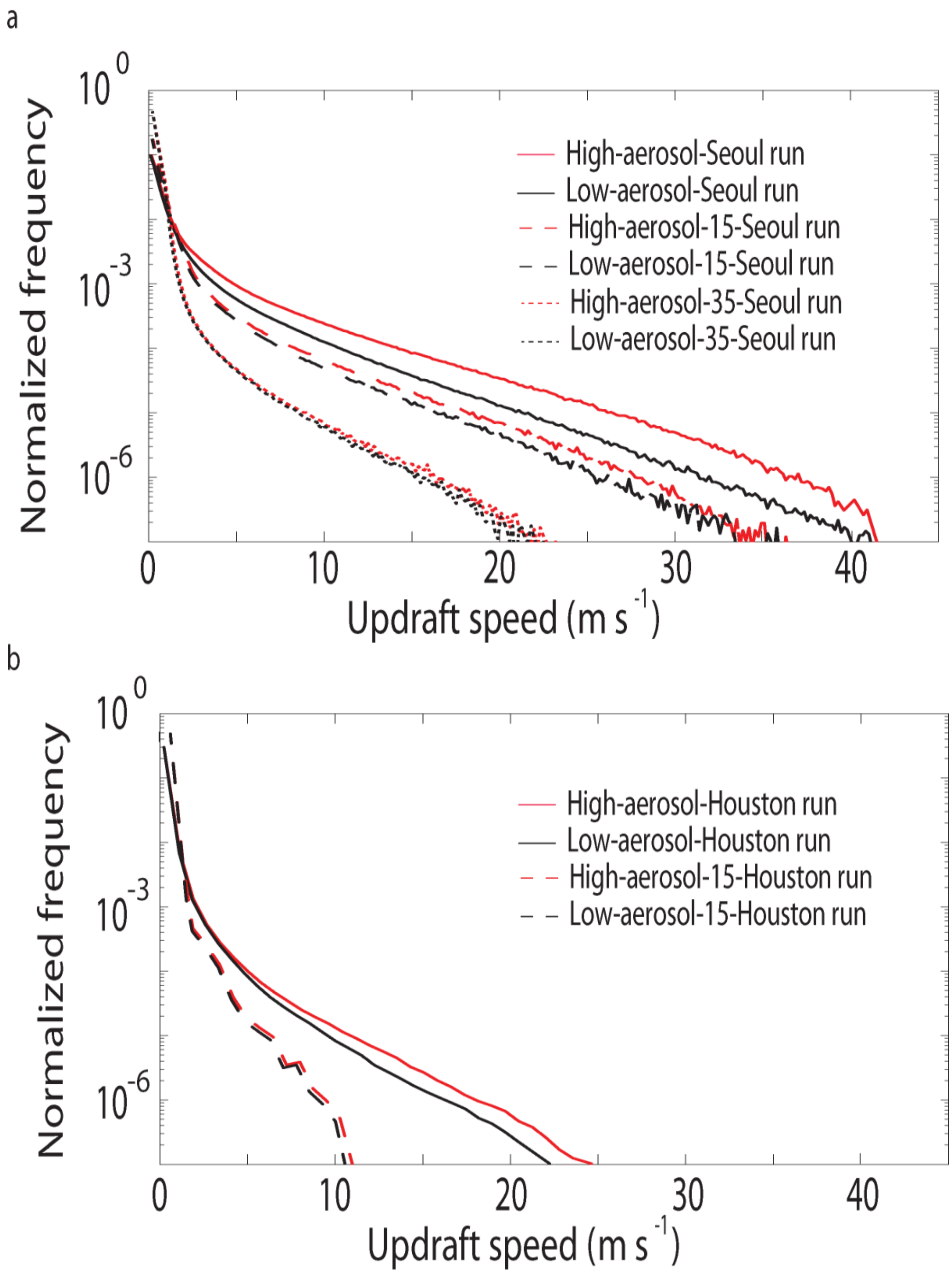
a
Normalized frequency
10^0
10^-3
10^-6
0
10
20
30
40
Updraft speed (m s^-1)
High-aerosol-Seoul run
Low-aerosol-Seoul run
High-aerosol-15-Seoul run
Low-aerosol-15-Seoul run
High-aerosol-35-Seoul run
Low-aerosol-35-Seoul run
b
Normalized frequency
10^0
10^-3
10^-6
0
10
20
30
40
Updraft speed (m s^-1)
High-aerosol-Houston run
Low-aerosol-Houston run
High-aerosol-15-Houston run
Low-aerosol-15-Houston run

Figure 10

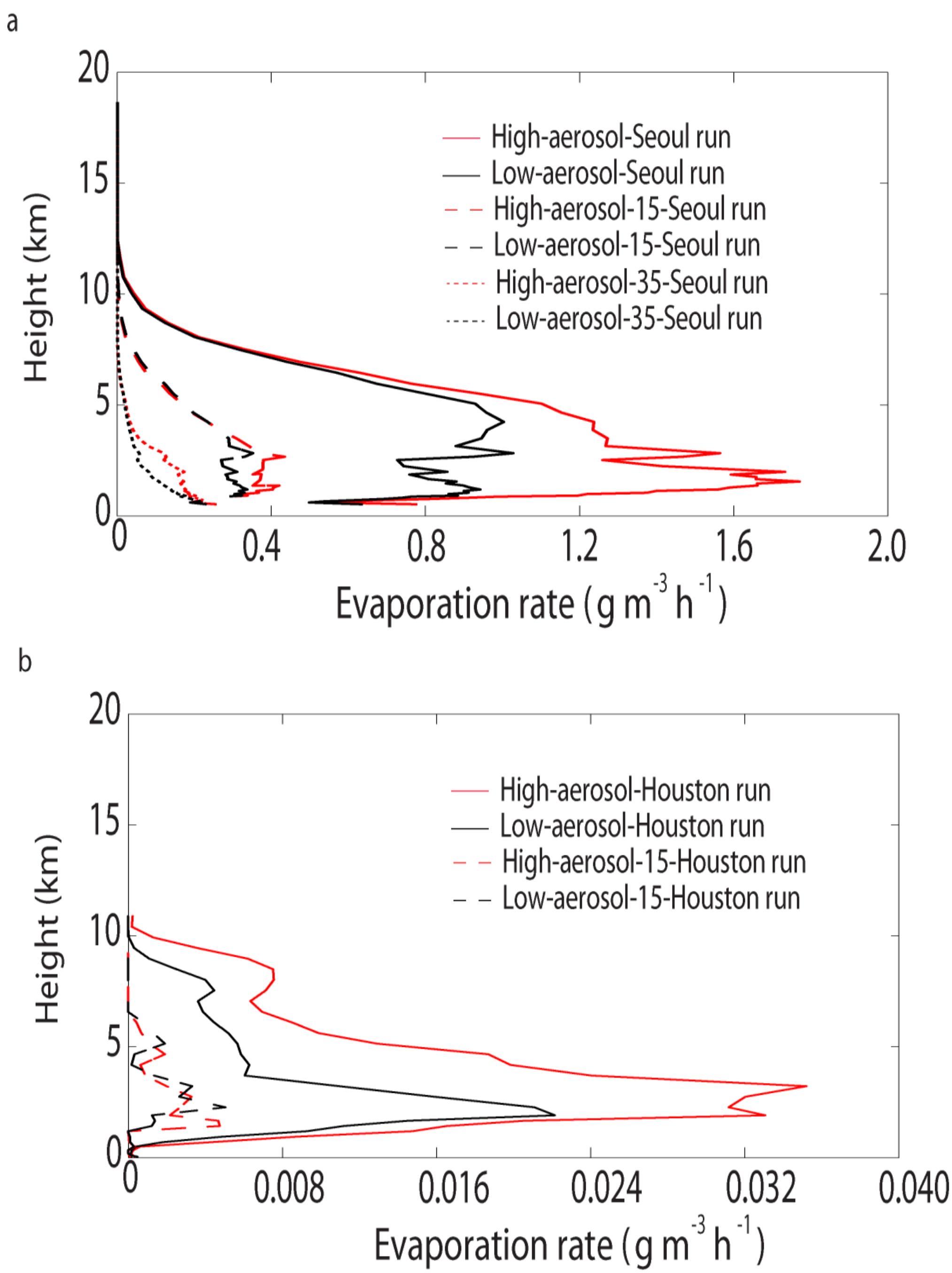
a
High-aerosol-Seoul run
Low-aerosol-Seoul run
High-aerosol-15-Seoul run
Low-aerosol-15-Seoul run
High-aerosol-35-Seoul run
Low-aerosol-35-Seoul run
Height (km)
0
5
10
15
20
0
0.4
0.8
1.2
1.6
2.0
Evaporation rate (g m-3 h-1)
b
High-aerosol-Houston run
Low-aerosol-Houston run
High-aerosol-15-Houston run
Low-aerosol-15-Houston run
Height (km)
0
5
10
15
20
0
0.008
0.016
0.024
0.032
0.040
Evaporation rate (g m-3 h-1)

Figure 11

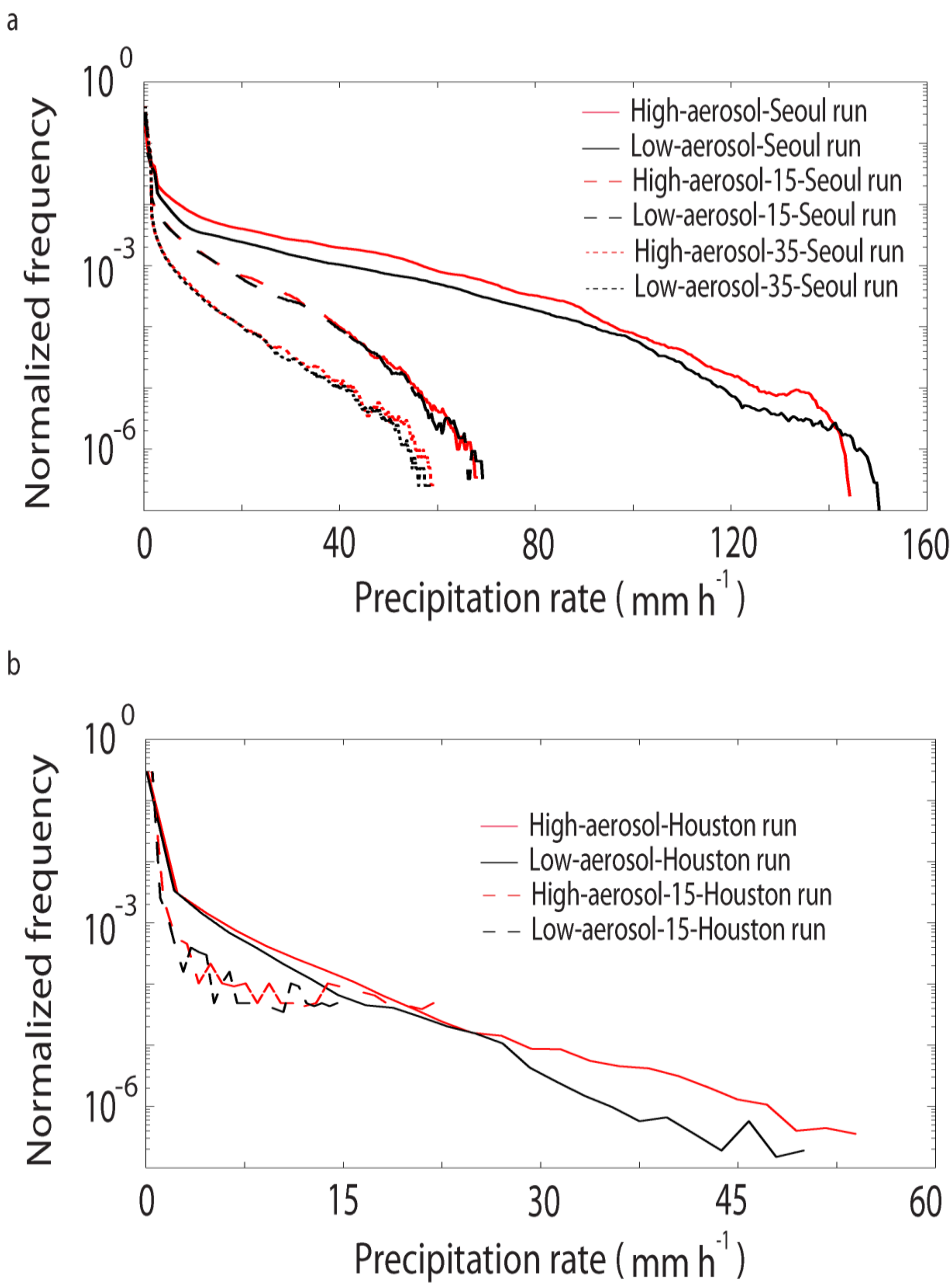
a
High-aerosol-Seoul run
Low-aerosol-Seoul run
High-aerosol-15-Seoul run
Low-aerosol-15-Seoul run
High-aerosol-35-Seoul run
Low-aerosol-35-Seoul run
Normalized frequency
10^0
10^-3
10^-6
0
40
80
120
160
Precipitation rate (mm h^-1)
b
High-aerosol-Houston run
Low-aerosol-Houston run
High-aerosol-15-Houston run
Low-aerosol-15-Houston run
Normalized frequency
10^0
10^-3
10^-6
0
15
30
45
60
Precipitation rate (mm h^-1)

Figure 12

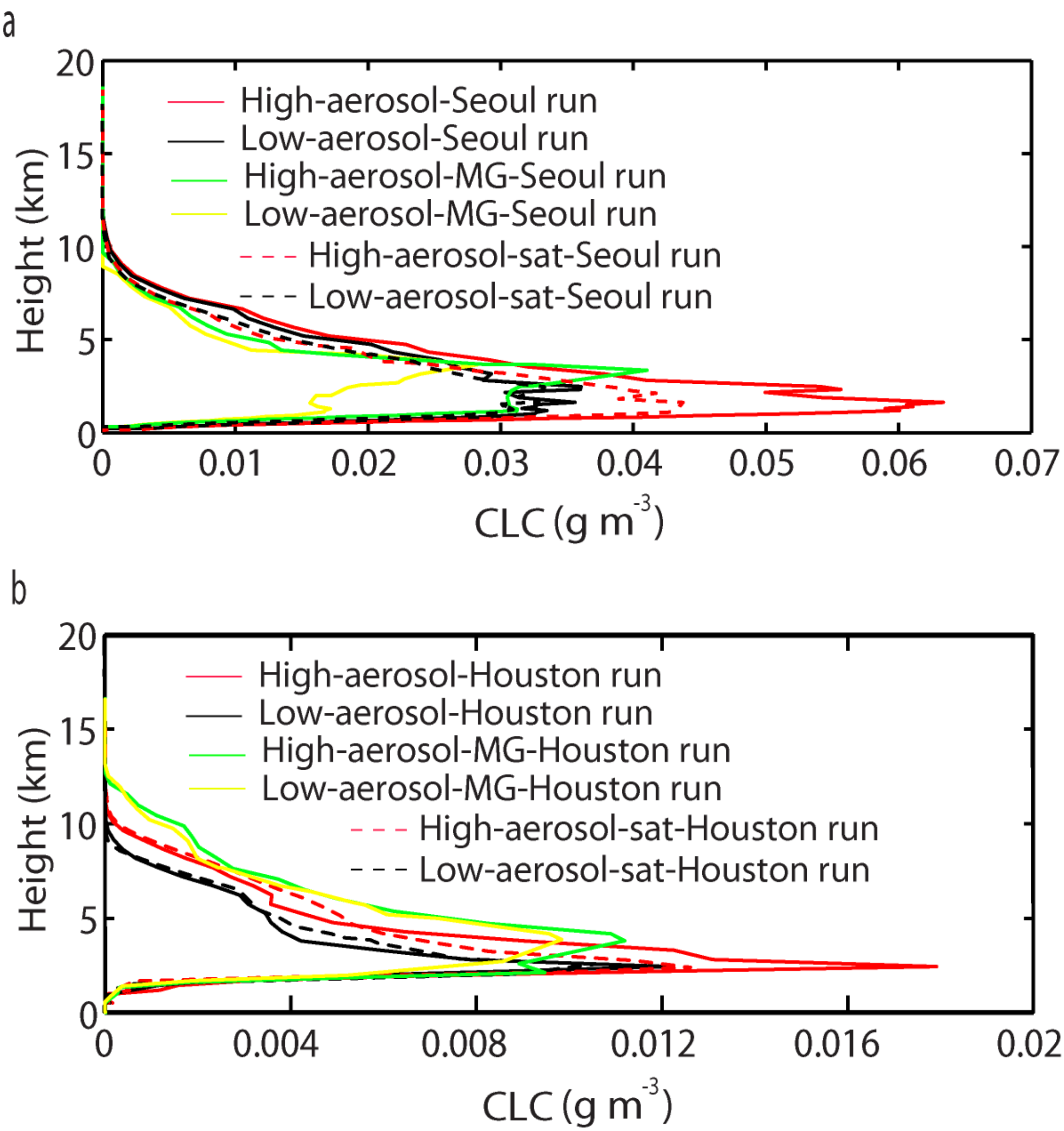
a
High-aerosol-Seoul run
Low-aerosol-Seoul run
High-aerosol-MG-Seoul run
Low-aerosol-MG-Seoul run
High-aerosol-sat-Seoul run
Low-aerosol-sat-Seoul run
Height (km)
20
15
10
5
0
0
0.01
0.02
0.03
0.04
0.05
0.06
0.07
CLC (g m-3)
b
High-aerosol-Houston run
Low-aerosol-Houston run
High-aerosol-MG-Houston run
Low-aerosol-MG-Houston run
High-aerosol-sat-Houston run
Low-aerosol-sat-Houston run
Height (km)
20
15
10
5
0
0
0.004
0.008
0.012
0.016
0.02
CLC (g m-3)

Figure 13

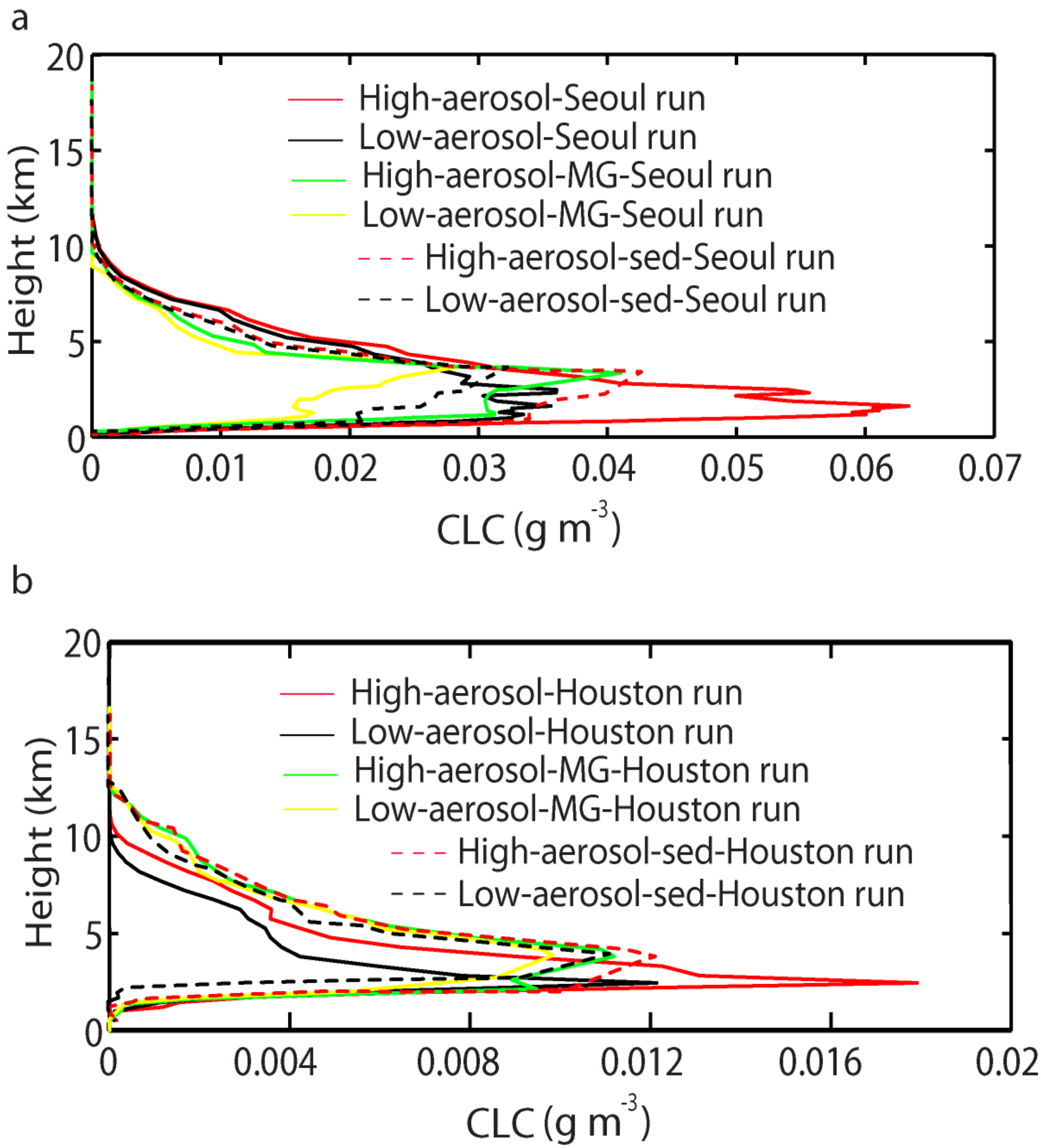
a
High-aerosol-Seoul run
Low-aerosol-Seoul run
High-aerosol-MG-Seoul run
Low-aerosol-MG-Seoul run
High-aerosol-sed-Seoul run
Low-aerosol-sed-Seoul run
Height (km)
0
5
10
15
20
0
0.01
0.02
0.03
0.04
0.05
0.06
0.07
CLC (g m^-3)
b
High-aerosol-Houston run
Low-aerosol-Houston run
High-aerosol-MG-Houston run
Low-aerosol-MG-Houston run
High-aerosol-sed-Houston run
Low-aerosol-sed-Houston run
Height (km)
0
5
10
15
20
0
0.004
0.008
0.012
0.016
0.02
CLC (g m^-3)

Figure 14

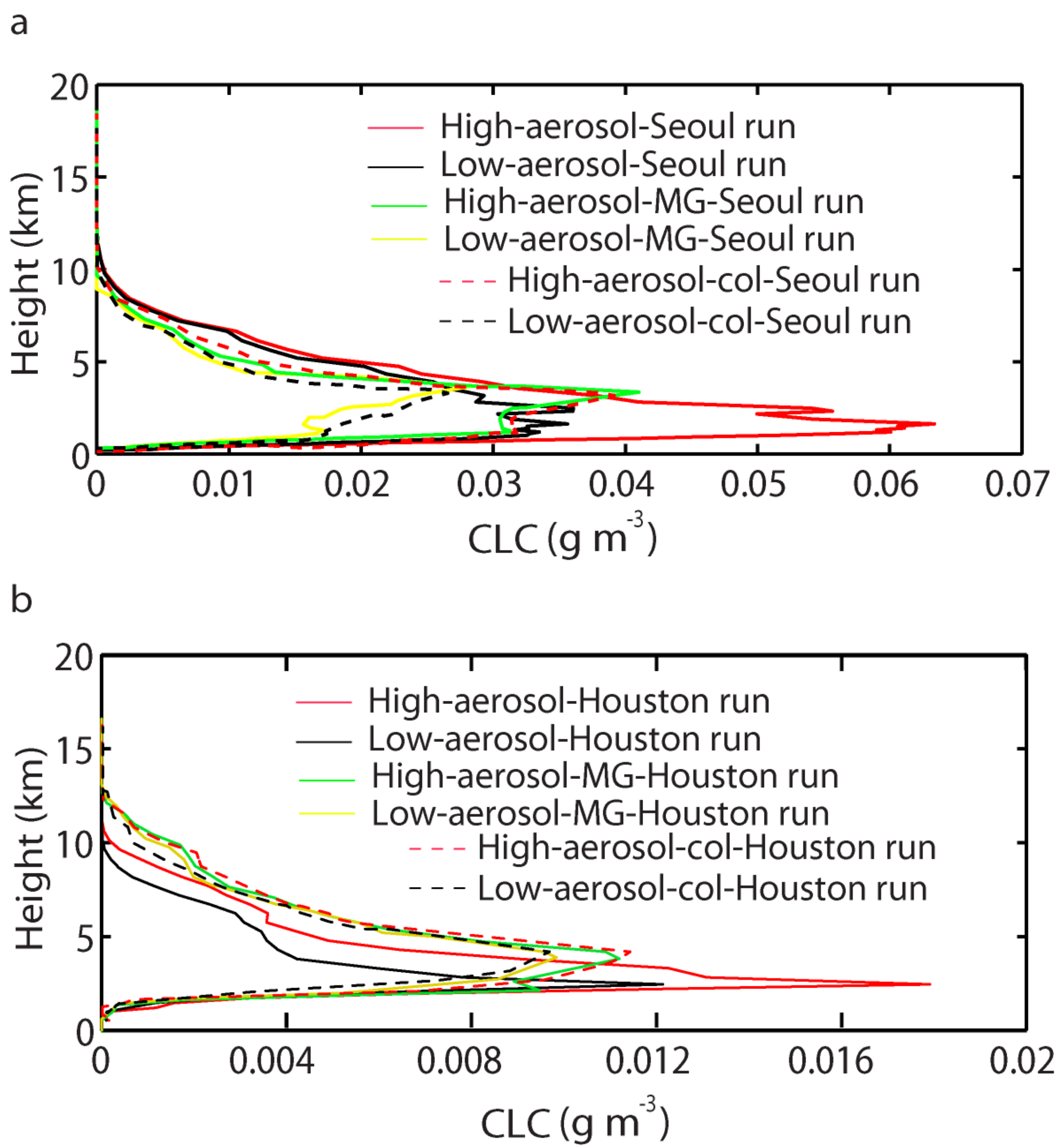
a
High-aerosol-Seoul run
Low-aerosol-Seoul run
High-aerosol-MG-Seoul run
Low-aerosol-MG-Seoul run
High-aerosol-col-Seoul run
Low-aerosol-col-Seoul run
Height (km)
0
5
10
15
20
0
0.01
0.02
0.03
0.04
0.05
0.06
0.07
CLC (g m^-3)
b
High-aerosol-Houston run
Low-aerosol-Houston run
High-aerosol-MG-Houston run
Low-aerosol-MG-Houston run
High-aerosol-col-Houston run
Low-aerosol-col-Houston run
Height (km)
0
5
10
15
20
0
0.004
0.008
0.012
0.016
0.02
CLC (g m^-3)

Figure 15